

Non-canonical glutamine transamination sustains efferocytosis by coupling redox buffering to oxidative phosphorylation

Citation for published version (APA):

Merlin, J., Ivanov, S., Dumont, A., Sergushichev, A., Gall, J., Stunault, M., Ayrault, M., Vaillant, N., Castiglione, A., Swain, A., Orange, F., Gallerand, A., Berton, T., Martin, J.-C., Carobbio, S., Masson, J., Gaisler-Salomon, I., Maechler, P., Rayport, S., ... Yvan-Charvet, L. (2021). Non-canonical glutamine transamination sustains efferocytosis by coupling redox buffering to oxidative phosphorylation. *Nature Metabolism*, 3(10), 1313-1326. <https://doi.org/10.1038/s42255-021-00471-y>

Document status and date:

Published: 01/10/2021

DOI:

[10.1038/s42255-021-00471-y](https://doi.org/10.1038/s42255-021-00471-y)

Document Version:

Publisher's PDF, also known as Version of record

Document license:

Taverne

Please check the document version of this publication:

- A submitted manuscript is the version of the article upon submission and before peer-review. There can be important differences between the submitted version and the official published version of record. People interested in the research are advised to contact the author for the final version of the publication, or visit the DOI to the publisher's website.
- The final author version and the galley proof are versions of the publication after peer review.
- The final published version features the final layout of the paper including the volume, issue and page numbers.

[Link to publication](#)

General rights

Copyright and moral rights for the publications made accessible in the public portal are retained by the authors and/or other copyright owners and it is a condition of accessing publications that users recognise and abide by the legal requirements associated with these rights.

- Users may download and print one copy of any publication from the public portal for the purpose of private study or research.
- You may not further distribute the material or use it for any profit-making activity or commercial gain
- You may freely distribute the URL identifying the publication in the public portal.

If the publication is distributed under the terms of Article 25fa of the Dutch Copyright Act, indicated by the "Taverne" license above, please follow below link for the End User Agreement:

www.umlib.nl/taverne-license

Take down policy

If you believe that this document breaches copyright please contact us at:

repository@maastrichtuniversity.nl

providing details and we will investigate your claim.



Non-canonical glutamine transamination sustains efferocytosis by coupling redox buffering to oxidative phosphorylation

Johanna Merlin^{1,17}, Stoyan Ivanov^{1,17}, Adélie Dumont^{1,17}, Alexey Sergushichev², Julie Gall¹, Marion Stunault¹, Marion Ayrault¹, Nathalie Vaillant¹, Alexia Castiglione¹, Amanda Swain³, Francois Orange⁴, Alexandre Gallerand¹, Thierry Berton⁵, Jean-Charles Martin⁵, Stefania Carobbio^{6,7,8}, Justine Masson^{9,10}, Inna Gaisler-Salomon^{10,11,12}, Pierre Maechler⁶, Stephen Rayport^{10,11}, Judith C. Sluimer¹³, Erik A. L. Biessen^{13,14}, Rodolphe R. Guinamd¹, Emmanuel L. Gautier¹⁵, Edward B. Thorp¹⁶, Maxim N. Artyomov³ and Laurent Yvan-Charvet¹✉

Macrophages rely on tightly integrated metabolic rewiring to clear dying neighboring cells by efferocytosis during homeostasis and disease. Here we reveal that glutaminase-1-mediated glutaminolysis is critical to promote apoptotic cell clearance by macrophages during homeostasis in mice. In addition, impaired macrophage glutaminolysis exacerbates atherosclerosis, a condition during which, efficient apoptotic cell debris clearance is critical to limit disease progression. Glutaminase-1 expression strongly correlates with atherosclerotic plaque necrosis in patients with cardiovascular diseases. High-throughput transcriptional and metabolic profiling reveals that macrophage efferocytic capacity relies on a non-canonical transaminase pathway, independent from the traditional requirement of glutamate dehydrogenase to fuel α -ketoglutarate-dependent immunometabolism. This pathway is necessary to meet the unique requirements of efferocytosis for cellular detoxification and high-energy cytoskeletal rearrangements. Thus, we uncover a role for non-canonical glutamine metabolism for efficient clearance of dying cells and maintenance of tissue homeostasis during health and disease in mouse and humans.

Clearance of apoptotic cells (ACs) by macrophages (efferocytosis) prevents the leakage of dying cellular contents to maintain tissue integrity in normal physiology^{1,2}. Impaired efferocytosis in disease can have multiple causes, but defects in the internalization of multiple ACs, a process termed ‘continual efferocytosis’, has emerged as a culprit of many chronic inflammatory diseases, such as atherosclerosis^{3,4}. Resolution and repair processes also require the cytokine interleukin (IL)-4 (ref. 5) and an efficient cellular metabolic reprogramming to sustain continual efferocytosis⁶. However, the understanding of metabolism during efferocytosis on a molecular level is still poorly understood and fundamentally and clinically relevant.

Glutamine metabolism is considered as a ‘fuel for the immune system’ and is routinely used as a component for clinical supplementation in trauma patients. Glutamine is initially hydrolyzed into glutamate by glutaminase-1 (GLS1) in a metabolic process called glutaminolysis^{7,8}, which is the most upregulated pathway in

reparative-type macrophages induced by IL-4-dependent alternative activation⁹. Yet whether glutaminolysis supports the functional metabolic reprogramming of efferocytosis beyond glucose and fatty acid metabolism remains unknown^{10,11}.

Here we tested the hypothesis that glutaminolysis plays a critical role in macrophage efferocytic capacity. Mice lacking macrophage *Glsl* exhibited defective efferocytosis in vivo and in vitro under reparative conditions or upon successive rounds of exposure to dying cells. The clinical and pathologic relevance of glutaminolysis in this process was exemplified with the inverse association with the accumulation of necrotic core in human and murine atherosclerotic lesions. Mechanistically, glutaminolysis channeled glutamate into the malate–aspartate shuttle through an aspartate aminotransferase (GOT)-dependent transamination process to meet the demand for cellular detoxification and cytoskeletal rearrangements and achieve efficient efferocytosis.

¹Institut National de la Santé et de la Recherche Médicale (Inserm) U1065, Université Côte d’Azur, Centre Méditerranéen de Médecine Moléculaire (C3M), Centre National de la Recherche Scientifique (CNRS) (R.G.), Atip-Avenir, Fédération Hospitalo-Universitaire (FHU) Oncoage, Nice, France.

²Computer Technologies Department, ITMO University, Saint Petersburg, Russia. ³Department of Pathology and Immunology, Washington University School of Medicine, St. Louis, MO, USA. ⁴Université Côte d’Azur, Centre Commun de Microscopie Appliquée (CCMA), Nice, France. ⁵Centre de Recherche Cardiovasculaire et Nutritionnelle (C2VN), INSERM, Institut National de la Recherche Agricole (INRA), BioMet, Aix-Marseille University, Marseille, France. ⁶Department of Cell Physiology and Metabolism, University of Geneva Medical Centre, Geneva, Switzerland. ⁷Wellcome Trust Sanger Institute, Wellcome Trust Genome Campus, Hinxton, UK. ⁸Metabolic Research Laboratories, Addenbrooke’s Treatment Centre, Institute of Metabolic Science, Addenbrooke’s Hospital, University of Cambridge, Cambridge, UK. ⁹Inserm UMR-S1270, Institut du Fer à Moulin, Sorbonne Université, Paris, France.

¹⁰Department of Molecular Therapeutics, NYS Psychiatric Institute, New York, NY, USA. ¹¹Department of Psychiatry, Columbia University, New York, NY, USA. ¹²SPC-IBBR, University of Haifa, Haifa, Israel. ¹³Department of Pathology, Cardiovascular Research Institute Maastricht, Maastricht University Medical Center, Maastricht, the Netherlands. ¹⁴Institute for Molecular Cardiovascular Research, RWTH Klinikum Aachen, Aachen, Germany. ¹⁵Sorbonne Université, INSERM, UMR_S 1166 ICAN, Paris, France. ¹⁶Department of Pathology, Northwestern University, Feinberg School of Medicine, Chicago, IL, USA.

¹⁷These authors contributed equally: J. Merlin, S. Ivanov, A. Dumont. ✉e-mail: yvancharvet@unice.fr

Results

Macrophage glutaminolysis orchestrates optimal efferocytosis.

To investigate metabolic roles of macrophage glutaminolysis during clearance functions, mice bearing a conditional allele for GLS1 (*Gls1^{fl/fl}*) in macrophages were generated by crossing to lysozyme M-Cre transgenic mice (*LysM-Cre*). *LysM-Cre* × *Gls1^{fl/fl}* peritoneal cavity macrophages (*Mac^{ΔGls1}* PCMs) efficiently deleted GLS1 and presented with a twofold decrease in cellular glutamate levels as compared to controls (Fig. 1a). Glutaminolysis can control the balance between cellular life and death in vitro through mTORC1 pathway or ferroptosis, respectively^{12,13}. Although *Gls1* was expressed to various levels in PCMs, bone marrow (BM) monocytes/macrophages, red pulp macrophages (RPMs), Kupffer cells and microglia (Extended Data Fig. 1a), their numbers were unaltered in *Mac^{ΔGls1}* mice (Extended Data Fig. 1b). Consistently, proliferation and apoptosis were similar in *Mac^{ΔGls1}* PCMs compared to control cells (Extended Data Fig. 1c). Levels of phospho-S6 and Myc protein, mTORC1 downstream targets, were also unchanged in these cells (Extended Data Fig. 1d) along with absence of transcriptional regulation of rapamycin (mTOR), hypoxia or ferroptosis targets (Extended Data Fig. 1e). These data strongly suggested that glutaminolysis is not required for macrophage maintenance or development at steady state. Consistent with the strong enrichment in glutaminolytic processes in IL-4-treated reparative macrophages⁹, we observed an impaired induction of canonical alternatively activated genes (*Clec10a*, *Tgm2*, *Arg1*, *Stab1* and *Sepp1*) (Extended Data Fig. 1f) and cell surface expression of CD206 and CD301 (Extended Data Fig. 1g) in *Mac^{ΔGls1}* PCMs. Additionally, challenging PCMs with either IL-4, ACs or IL-4 and ACs together revealed that GLS1-dependent glutaminolysis was required for efficient efferocytosis in reparative macrophages. We measured an approximately 20% phagocytic index reduction in IL-4-stimulated *Mac^{ΔGls1}* TIMD4⁺ PCM subsets after 45 min exposure to apoptotic thymocytes (Fig. 1b). A similar trend was observed in the less-efferocytic TIMD4⁻ PCM subset (Fig. 1b). This occurred independently of transcriptional changes in key efferocytic receptors such as *Mertk*, *Timd4* or *Gas6* or immunoregulatory cytokines such as *Tgfb* or *Il10* in reparative *Mac^{ΔGls1}* PCMs (Extended Data Fig. 1h). Consistently, IL-10 secretion levels were unaltered in these cells (Extended Data Fig. 1h). Nevertheless, these responses were specific of AC clearance as similar percentage of heat-killed *Escherichia coli* phagocytosis was observed between control and *Mac^{ΔGls1}* PCMs (Extended Data Fig. 1i). Defects in efferocytic responses were also confirmed using IL-4-primed reparative BM-derived macrophages (BMDMs) (Fig. 1c). Notably, overexpression of *Gls1* in BMDMs using lentiviral particles enhanced efferocytosis in unstimulated control cells and rescued the defective efferocytosis observed in reparative *Mac^{ΔGls1}* macrophages (Fig. 1d). To test the impact of glutaminolysis on efferocytosis during heightened metabolic challenge, we subjected *Gls1*-deficient macrophages to successive rounds of AC clearance, which mimics tissue states of high cell turnover⁶. We performed a validated two-stage efferocytosis experiment in which BMDMs were first incubated for 45 min with unlabeled ACs and, after AC removal and a 1-h interval, incubated with a second round of labeled ACs³. Under these conditions, the percentage of resolving macrophages that had internalized the second round of ACs was significantly decreased in *Gls1*-deficient macrophages relative to controls (Fig. 1e). To test the in vivo significance, we intravenously (i.v.) injected fluorescently labeled ACs into controls and *Mac^{ΔGls1}* mice. *Gls1* deficiency reduced the ability of CD11b^{lo}F4/80^{high} Kupffer cells (KCs) in the liver and RPMs in the spleen and to some extent CD11b^{high}F4/80^{high} monocyte-derived macrophages (MoMacs) to internalize labeled ACs 1 h after injection (Fig. 1f). These findings provide in vivo genetic evidence of the pivotal role of GLS1-dependent glutaminolysis during macrophage phagocytic clearance.

Glutaminolysis regulates efferocytosis in atherosclerosis. We next tested GLS1 requirements in a mouse model of atherosclerosis, in which defective lesional dead cell clearance translates into unstable necrotic core within plaques¹⁴. Taking advantage of publicly available gene expression datasets of western diet (WD)-fed wild-type (WT) and *Apoe*-deficient mice¹⁵, we observed down-regulation of *Gls1* expression in atheromatous plaques. This was part of a dysregulated amino acid catabolism module making up a densely connected core with a more global metabolic transcriptome signature (Extended Data Fig. 2a). Lower *Gls1* expression correlated with an imbalance in markers of inflammatory and reparative macrophages (heat map; Extended Data Fig. 2a). To monitor glutaminolysis activity in atherosclerotic plaque, we next assessed radiolabeled [¹⁴C] glutamine uptake and hydrolysis in aortas extracted from WT and *Apoe*^{-/-} mice fed a WD for 6 weeks. Biomolecular imaging revealed higher glutamine incorporation into plaque areas enriched in macrophages (Extended Data Fig. 2b). Nevertheless, quantification of [¹⁴C] glutamine conversion into glutamate, after separation by thin-layer chromatography (TLC), confirmed lower glutaminase-dependent metabolism in atherosclerotic aorta (Extended Data Fig. 2c). Next, mice with macrophage-specific deletion of *Gls1* (*Mac^{ΔGls1}* mice) were crossed onto an atherosclerotic *Apoe*-deficient background. After WD feeding (12 weeks), there was an approximately 1.7-fold increase in atherosclerosis plaque area in the aortic sinus compared to co-housed control littermates (Fig. 2a). Oil Red O staining in descending aortas confirmed higher plaque burden in *Apoe*^{-/-} *Mac^{ΔGls1}* mice (Fig. 2b) despite similar plasma lipid levels (Extended Data Fig. 2d). Increased plaque area was also visualized in an independent cohort of *Apoe*^{-/-} *Mac^{ΔGls1}* mice using noninvasive ultrasound imaging (Fig. 2c). These effects were specific to macrophage glutaminolysis because hematopoietic *Gls1* deficiency (generation of *Mx1-Cre* × *Gls1^{fl/fl}* mice onto the atherosclerotic *Apoe*^{-/-} background, referred as *Apoe*^{-/-} HSC^{ΔGls1} mice) recapitulated similar accelerated atherosclerosis relative to control animals (Extended Data Fig. 2e). Further characterization of atherosclerotic lesions in *Apoe*^{-/-} *Mac^{ΔGls1}* mice revealed complex plaques containing macrophages (Extended Data Fig. 2f). We did not observe a marked change in Ki67-positive proliferative cells in *Apoe*^{-/-} *Mac^{ΔGls1}* mice (Extended Data Fig. 2f). In contrast, necrotic cores were typified by a greater proportion of TUNEL-positive free ACs and a reduced proportion of macrophage-associated ACs, a hallmark of defective efferocytosis (Fig. 2d). By injecting fluorescent dye-labeled apoptotic lymphocytes intraperitoneally, we confirmed the reduced ability of peritoneal macrophages from *Apoe*^{-/-} *Mac^{ΔGls1}* mice to efficiently perform efferocytosis (Extended Data Fig. 2g). To examine clinical significance, we investigated whether *Gls1* expression correlated with human atherosclerotic plaque complexity. We found a reduced *Gls1* expression in unstable versus stable human carotid artery plaque (Fig. 2e). Moreover, we uncovered a positive correlation between *Gls1* expression and the M2-specific marker Arg1⁺ (Fig. 2e). By contrast, *Gls1* levels inversely correlated with plaque size, intraplaque hemorrhage and necrotic core composition (Fig. 2e), key markers of atherosclerosis severity. Taken together, our findings demonstrate that GLS1 contributes to AC engulfment in the pathological process of human and murine atherosclerosis.

Glutaminolysis supports efferocytosis by fueling OxPHOS.

We next found that intracellular *Gls1* mRNA expression was similarly upregulated by IL-4 stimulation or AC ingestion in a validated gene expression dataset (Extended Data Fig. 3a)⁵. We confirmed this upregulation in a time course experiment (Extended Data Fig. 3b), paralleling a drop in cellular glutamine to glutamate ratio (Extended Data Fig. 3c). To identify how glutamine-dependent pathways are regulated in reparative macrophages, we traced ¹³C-labeled glutamine intracellular fate and quantified several metabolites and by-products by liquid chromatography–mass spectrometry

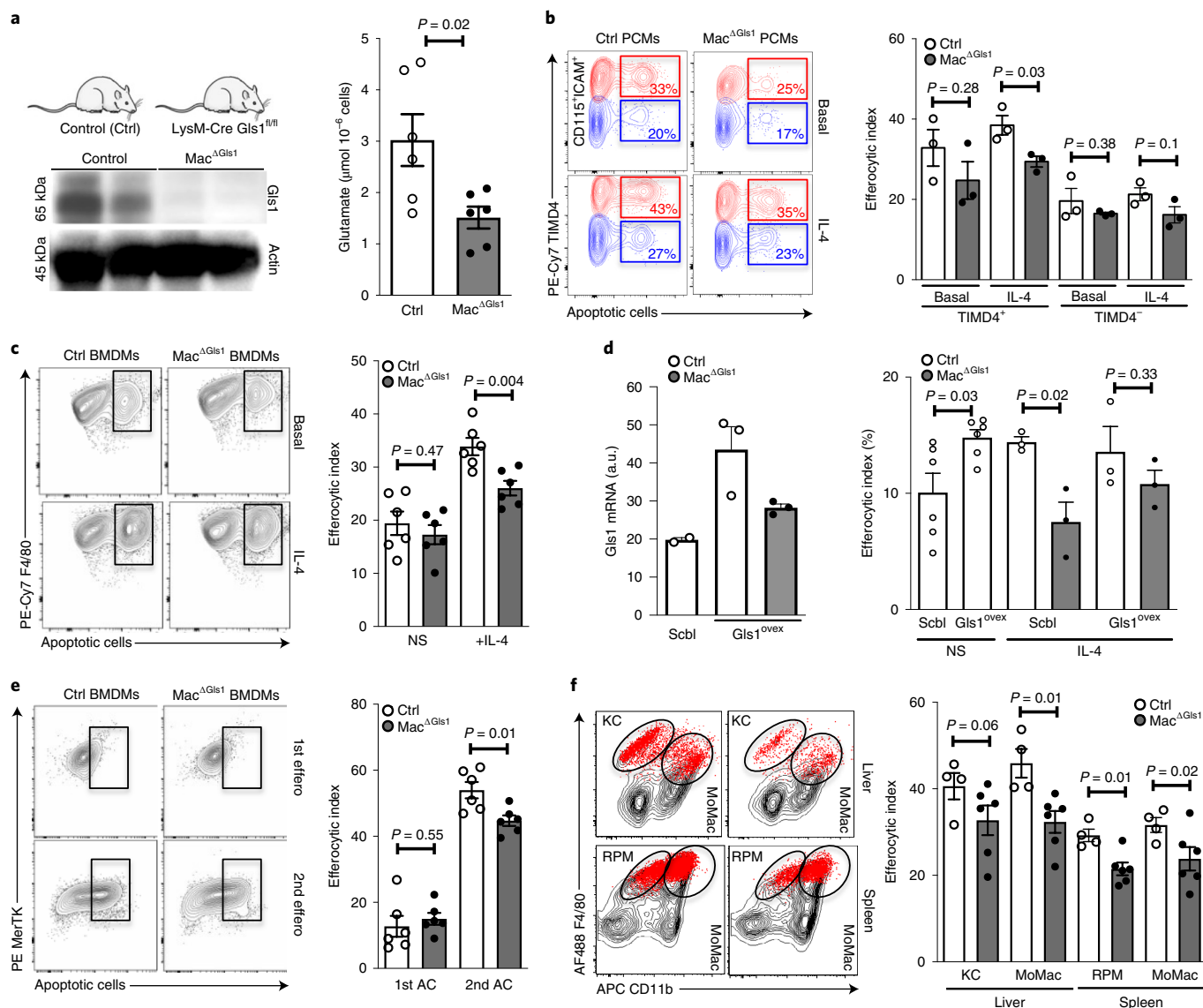


Fig. 1 | Macrophage *Gls1* deletion impairs efferocytosis in vitro and in vivo. **a**, Western blot of GLS1 protein (left) and glutamate levels (right) in *Gls1^{fl/fl}* control and Mac ^{Δ Gls1} PCMs. **b**, Efferocytic index gating strategy (left) and quantification (right) measured by flow cytometry after 45 min exposure with ACs in Cre⁺ control and Mac ^{Δ Gls1} PCMs at steady state (resting condition) or after overnight IL-4 stimulation (reparative condition). **c**, Similar experiments were performed in resting and reparative control (both *Gls1^{fl/fl}* and Cre⁺) and Mac ^{Δ Gls1} BMDMs. Efferocytic index was calculated as (number of macrophages with ACs / total number of macrophages) \times 100. **d**, qPCR quantification (left) and efferocytic index (right) in *Gls1^{fl/fl}* control and Mac ^{Δ Gls1} BMDMs stimulated overnight with IL-4 after *Gls1* lentivirus overexpression. **e**, Efferocytic index gating strategy (left) and quantification (right) measured by flow cytometry after one (45 min) or two (45 min + 1-h rest + 45 min) incubations with ACs (resolving condition) in control (both *Gls1^{fl/fl}* and Cre⁺) and Mac ^{Δ Gls1} BMDMs. **f**, Efferocytic index gating strategy (left) and quantification (right) measured by flow cytometry in *Gls1^{fl/fl}* control and Mac ^{Δ Gls1} KCs, RPMs and MoMacs after labeled apoptotic thymocytes i.v. injection. Both sexes were analyzed. All values are mean \pm s.e.m. and are representative of at least one independent experiment ($n = 6$ independent animals (**a, c, e**), $n = 3$ to 6 (**d**), $n = 3$ (**b**)). Western blot results in **a** are representative experiments of two biologically independent replicates. *P* values were determined by two-tailed Student's *t*-test. Source data are provided as a Source Data file (**a–f**).

(LC–MS). Labeling distribution analyses revealed similar ¹³C incorporation into branched-chain amino acid (BC-AA), proline, glutamate- γ semialdehyde (GSA), arginine and ornithine in reparative Mac ^{Δ Gls1} BMDMs, indicative of similar BC-AA catabolism and urea cycle turnover (Fig. 3a and Supplementary Table. 1). Consistently, similar levels of these compounds (leucine, valine, ornithine, arginine, proline and putrescine) were observed in Mac ^{Δ Gls1} BMDMs (Extended Data Fig. 3d,e) and inhibition of BB-AA transferase with gabapentin or branched-chain amino acid transaminase (BCAT) 1 or supplementation with ornithine had no impact on the efferocytic response of reparative Mac ^{Δ Gls1} BMDMs (Extended

Data Fig. 3f). By contrast, lower ¹³C incorporation into tricarboxylic acid (TCA) metabolites (α -ketoglutarate (α -KG), succinate, malate and aspartate but not citrate or aconitate) was observed in reparative Mac ^{Δ Gls1} BMDMs, supporting partially defective TCA cycling in these cells (Fig. 3a). We next provided evidence of reduced basal oxygen consumption rate (OCR) and maximal respiration after carbonyl cyanide-*p*-trifluoromethoxyphenylhydrazone (FCCP) treatment in Mac ^{Δ Gls1} PCMs and BMDMs in comparison to control cells (Extended Data Figs. 3g,h). These effects occurred independently of fluctuation in extracellular acidification rate (ECAR), a surrogate of glycolytic activity (Extended Data Fig. 3i). Additionally, reduced

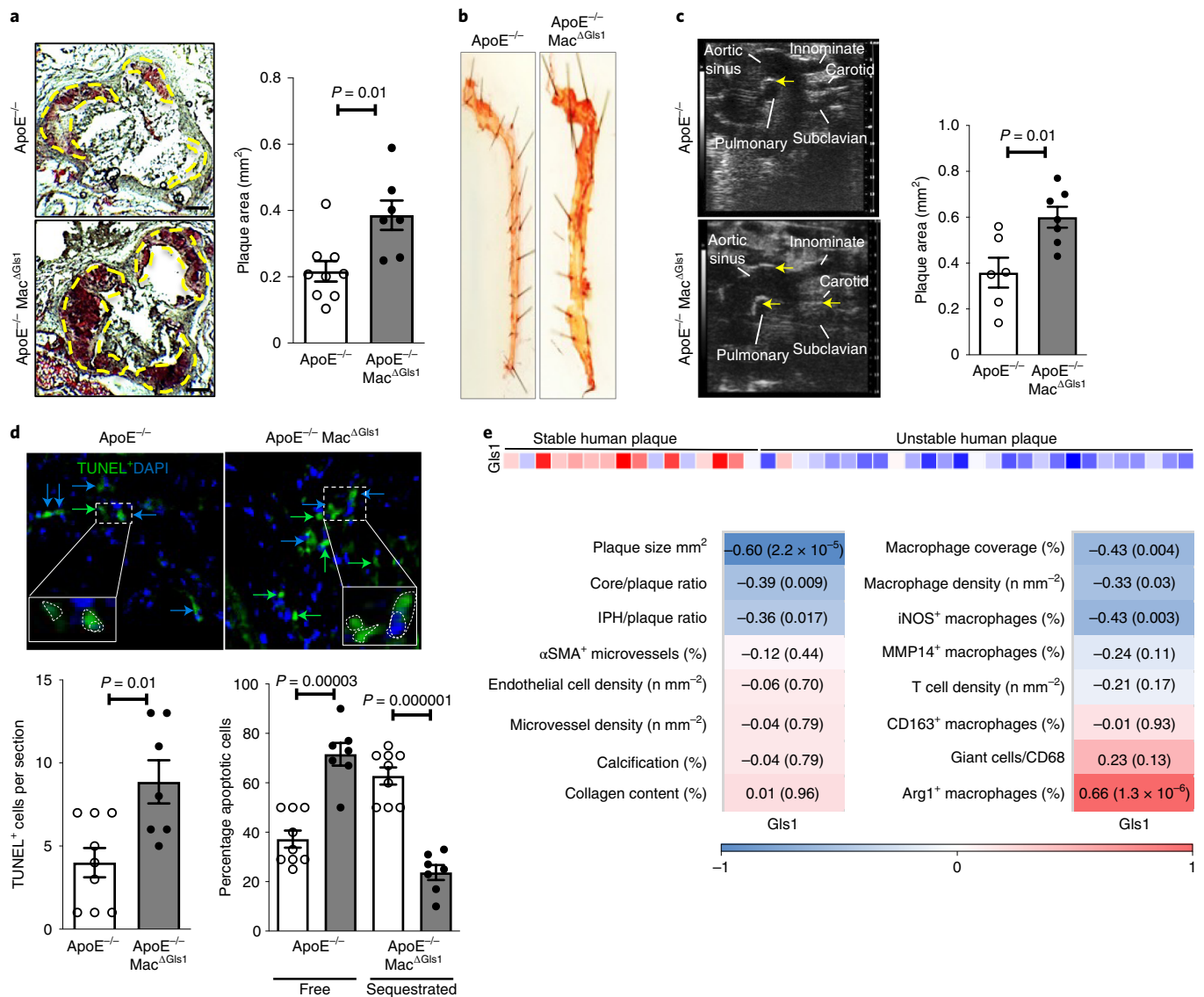


Fig. 2 | Myeloid-*Gls1* deletion impairs efferocytosis in the pathological process of atherosclerosis. **a**, Representative sections (left) and quantification (right) of aortic plaques from *ApoE*^{-/-} or *ApoE*^{-/-} *Mac*^{Δ*Gls1*} mice (12 weeks WD) stained for Oil Red O and hematoxylin and eosin (H&E). Scale bar, 200 μm. Both sexes were analyzed. **b**, Oil Red O-stained descending aortas from representative female *ApoE*^{-/-} or *ApoE*^{-/-} *Mac*^{Δ*Gls1*} mice maintained on a WD for 12 weeks. **c**, Echography (left) and quantification (right) of aortic plaques from male *ApoE*^{-/-} or *ApoE*^{-/-} *Mac*^{Δ*Gls1*} mice fed for 12 weeks on WD. Arrows indicate plaque areas. **d**, Representative images (top) and quantification (bottom) of TUNEL⁺ cells (green) in aortic plaques from *ApoE*^{-/-} or *ApoE*^{-/-} *Mac*^{Δ*Gls1*} mice (12 weeks WD). Sections were counterstained with 4,6-diamidino-2-phenylindole (DAPI) (blue). TUNEL-positive AC as free (TUNEL-positive considered as apoptotic bodies) or cell sequestered (TUNEL-positive associated with large cellular nuclei considered as efferocytes) was quantified. All values are mean ± s.e.m. and are representative of at least one independent experiment (*n* = 6 to 9 independent animals for **a,c,d**). *P* values were determined by two-tailed Student's *t*-test. Source data are provided as a Source Data file (**a,c,d**). **e**, Correlation between *Gls1* expression and human atherosclerotic plaque complexity in the Maastricht Pathology collection (Results are from 16 stable segments and 27 unstable segments; red indicates positive correlations and blue indicates negative correlations).

mitochondrial complex I (NADH-ubiquinone oxidoreductase) and complex II (succinate dehydrogenase (SDH)) activities were observed in reparative *Mac*^{Δ*Gls1*} BMDMs (Extended Data Fig. 3j). Flux measurements also showed that resting and reparative *Mac*^{Δ*Gls1*} BMDMs fed ACs exhibited a decrease in maximal respiration response (Fig. 3b,c). These effects were associated with a drop in ATP production reflecting an inability to fully respond to the increase in energy demand (Fig. 3d). Basal OCR and maximal respiration response were also reduced in *Gls1*-deficient macrophages during continued clearance of ACs (Extended Data Fig. 3k). Inversely, lentiviral vector-mediated overexpression of *Gls1* enhanced OCR (Extended Data Fig. 3l) and ATP production (Extended Data

Fig. 3m) in control macrophages and partially rescued defects observed in reparative *Mac*^{Δ*Gls1*} BMDMs.

Glutaminolysis induces efficient ETC during efferocytosis. The observed altered mitochondrial metabolism in resting and reparative *Mac*^{Δ*Gls1*} BMDMs was associated with higher mitochondrial reactive oxygen species (ROS) levels (Extended Data Fig. 3n) and overexpression of *Gls1* conversely limited mitochondrial ROS production (Extended Data Fig. 3o). Mitochondrial redox status has been previously shown to metabolically program macrophage effector function^{16,17}. Thus, we next addressed whether it could be at the origin of the defective OCR in *Gls1*-deficient macrophages. Ectopic

expression of the mitochondrial alternative oxidase (AOX) from *Ciona intestinalis* improves the ubiquinone (CoQ) oxidoreduction balance by limiting buildup of electrons without pumping protons for ATP synthesis (Fig. 3e)^{18,19}. Overexpression of AOX abrogated the excess mitochondrial ROS production observed in reparative Mac^{ΔGls1} BMDMs (Fig. 3f) but did not rescue the defective OCR or ATP production in these cells (Fig. 3g and Extended Data Fig. 3p). These findings suggest that mitochondrial ROS is unlikely the cause but rather a ‘by-products’ of the defective oxidative phosphorylation (OxPHOS) in *Gls1*-deficient macrophages. Additionally, mitochondrial ROS scavenging by the superoxide dismutase mimetic (Tempol) or the mitochondria-targeted antioxidant coenzyme Q10 (MitoQ) (Fig. 3e) reduced mitochondrial ROS production to the same level between genotypes (Fig. 3h), but this was insufficient to rescue the defective OCR (Fig. 3i) and efferocytic index (Fig. 3j) of reparative Mac^{ΔGls1} BMDMs. In contrast, direct OCR inhibition by targeting SDH with 3-nitropropionic acid (3NPA) or complex III with antimycin A (Fig. 3i), enhanced ROS generation in the mitochondria (Fig. 3h) but reduced efferocytosis in control cells to the levels of reparative Mac^{ΔGls1} BMDMs (Fig. 3j). Similar findings were observed during continued clearance of ACs (Extended Data Fig. 3q). Consistent with the reduced OCR of Risp knockout macrophages¹¹, we also confirmed the genetic requirement of complex III to efferocytosis and continued clearance of ACs (Extended Data Fig. 3r). Together, these findings reveal that glutaminolysis couples mitochondrial oxidative phosphorylation to ATP production for efficient efferocytosis.

Topological analysis of metabolic networks. To elucidate the origin of the mitochondrial reprogramming in *Gls1*-deficient macrophage (Fig. 4a)²⁰, we performed an RNA sequencing (RNA-seq) analysis of PCMs stimulated by IL-4 *in vivo*. Metabolic pathway-enrichment analysis highlighted downregulation of oxidative phosphorylation and glutathione (GSH) synthesis KEGG pathways (NADP, folate and GSH metabolism) in resting and reparative Mac^{ΔGls1} PCMs (Fig. 4b). Thus, to dissect the interplay between the mitochondrial metabolic repurposing and the perturbation in antioxidant metabolism in Mac^{ΔGls1} macrophages, we next performed topological analyses using CoMBI-T profiling⁹ and compared predictions to DreamBio, which allows direct computational KEGG pathway mapping. CoMBI-T and DreamBio profiling analyses featured a link between Mac^{ΔGls1} PCM mitochondrial metabolic reprogramming and lower expression of TCA cycle and aspartate-arginino-succinate (AAS) shunt genes. These genes are interconnected to metabolism of glutamine per se, carbohydrates, hexosamine and fatty acids (Extended Data Fig. 4a,b). CoMBI-T predictions also revealed that the redox status of reparative Mac^{ΔGls1} PCMs may connect to the one carbon cycle-centered module known to support the transsulfuration pathway (GSH synthesis) (Extended Data Fig. 4a). KEGG mapping with DreamBio offered an alternative visualization of the perturbed transcriptomic pathways in reparative *Gls1*-deficient macrophages

and highlighted additional reactions that were not yet predicted (Extended Data Fig. 4b). For instance, in contrast to CoMBI-T, DreamBio analysis predicted downregulation of phosphoglucuronate dehydrogenase (*Pgd*) and malic enzyme (*Me1*) in reparative *Gls1*-deficient macrophages. These are two genes encoding enzymes that contribute to GSH salvage pathway through NADPH generation to efficiently supply reduced glutathione and maintain macrophage redox status (Extended Data Fig. 4b). Altogether, this unique approach helped to pinpoint the metabolic origin on how GLS1-dependent glutamine metabolism can integrate canonical mitochondrial reprogramming (TCA and AAS shunt) and non-canonical redox status (GSH synthesis and GSH salvage pathway) to support macrophage reparative function.

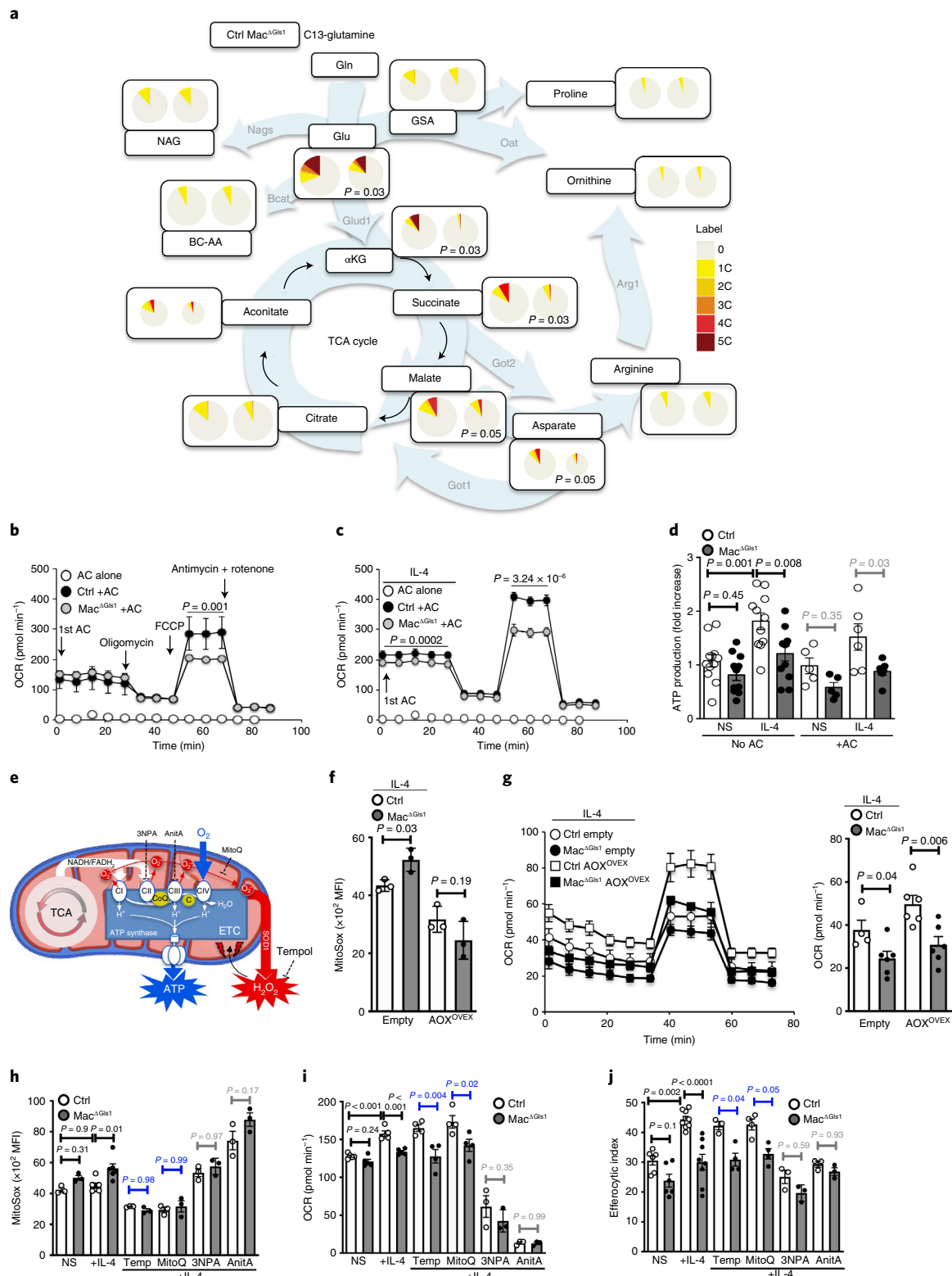
Canonical glutamine catabolism does not potentiate efferocytosis. To validate predictions of topological analyses, we next scrutinized utilization of glutamate into the canonical glutaminolysis pathway, which relies on glutamate dehydrogenase (GLUD1) to fuel α -KG into the TCA cycle (Fig. 4a). Inhibition of GLUD1 with epigallocatechin gallate (EGCG) raised basal OCR in reparative control macrophages but was not sufficient to rescue *Gls1*-deficient macrophage phenotypes (Fig. 4c). Treatment with EGCG also raised efferocytosis and ATP production (Fig. 4c and Extended Data Fig. 5a). Consistently, α -KG-dependent KDM6 and ten-eleven translocation dioxygenase 2 (TET2) activities were similar between control and Mac^{ΔGls1} BMDMs (Extended Data Fig. 5b). Treatment of control and Mac^{ΔGls1} BMDMs with dimethyl α -KG did also not rescue the inhibitory effect of *Gls1* deficiency on basal OCR (Extended Data Fig. 5c). Thus, the reduced glutamate levels in *Gls1*-deficient macrophages must impact non-canonical glutaminolysis pathways. To genetically validate these findings, we generated macrophage deficient for *Glud1* from mice lacking *Glud1* in hematopoietic cells (Extended Data Fig. 5d). In contrast to *Gls1* deficiency, higher basal OCR and maximal respiration response (Fig. 4d), ATP production rate (Fig. 4e) and efferocytosis (Fig. 4f) were measured in reparative *Glud1*-deficient macrophages. Thus, the reduced ATP production in *Gls1*-deficient macrophages is unlikely the consequence of reduced glutamate utilization into the canonical GLUD1-dependent glutaminolysis to fuel the TCA cycle.

Non-canonical glutamine transamination supports efferocytosis. We next investigated how perturbation of glutamate production connects non-canonical AAS shunt and oxidant stress to mitochondrial function in *Gls1*-deficient macrophages through pharmacological approaches and functional testing (Fig. 4a). Replenishment of the non-canonical GSH synthesis pathway with *N*-acetylcysteine (NAC) to prevent ATP leakage by limiting γ -glutamyl futile cycle synthesis⁷, had no effect on either OCR, ATP production or efferocytosis in Mac^{ΔGls1} BMDMs (Fig. 4c and Extended Data Fig. 5a). Indeed, a role of this futile cycle was unlikely as we also observed similar amounts of the pyroglutamate

Fig. 3 | Glutamine metabolism fuels mitochondrial OxPHOS to support efferocytosis. **a**, Carbon fluxes using U-¹³C-glutamine. U-¹³C glutamine was added in the medium of reparative IL-4 treated macrophages for 4 h. Circle sizes are scaled with respect to pool size for individual metabolites and the number of carbon incorporated from U-¹³C glutamine is indicated by color code. Thin black arrows represent known metabolic pathway connections; background arrows indicate deduced major metabolic flows in reparative macrophages. Gray to dark red indicate increased number of carbons. **b,c**, OCR measured by Seahorse after one incubation with ACs in control or Mac^{ΔGls1} BMDMs in resting conditions (**b**) or stimulated overnight with IL-4 (**c**). **d**, ATP production measured by Seahorse in resting and reparative control or Mac^{ΔGls1} BMDMs after one or no round of efferocytosis. **e**, Schematic representation of mitochondria ETC and its pharmacological inhibitors. **f**, Mitochondrial ROS quantification using MitoSox by flow cytometry in reparative control or Mac^{ΔGls1} BMDMs after lentiviral vector-mediated overexpression of mitochondrial AOX from *Ciona intestinalis*. **g**, OCR measured by Seahorse in these cells. **h-j**, MitoSox quantification (**h**), OCR quantification (**i**) and efferocytic index (**j**) in control or Mac^{ΔGls1} BMDMs at steady state or after overnight IL-4 stimulation \pm Tempol, mitoquinol, 3NPA or antimycin A. All values are mean \pm s.e.m. and are representative of at least one experiment ($n=6$ (**a**), $n=5$ to 12 (**b-d**), $n=3$ (**f-h**), $n=3$ to 9 (**i,j**) of biologically independent replicates). *P* values were determined by ordinary two-tailed Student's *t*-test (**a-c,f,g**) or one-way analysis of variance (ANOVA) with Tukey post hoc test for multiple comparisons (**d-h-j**). Each statistical bar color-coded represents an independent one-way ANOVA test. Source data are provided as a Source Data table (**a**) or Source Data file (**b-d,f-j**).

intermediate (also known as PCA or 5-oxoproline) in *Mac*^{ΔGls1} BMDMs (Extended Data Fig. 5e). In strong contrast, inhibition of the non-canonical aspartate aminotransferases (GOT_s)-dependent transamination with aminoxyacetic acid (AOA) reduced basal OCR, ATP production and this limited efferocytosis in control macrophages to the levels of reparative *Mac*^{ΔGls1} BMDMs (Fig. 4c and Extended Data Fig. 5a). Treatment with AOA also inhibited efferocytosis during continued clearance of ACs in resolving

control and *Mac*^{ΔGls1} BMDMs (Extended Data Fig. 5f) or in reparative *Glud1*-deficient BMDMs (Fig. 4f). We validated these observations by showing that reduced expression of *Got1* and *Got2* by siRNA in BMDMs prevented the engulfment of ACs (Extended Data Fig. 5g). Thus, the reduced ATP production in *Gls1*-deficient macrophages is the consequence of reduced glutamate utilization into the non-canonical transaminase-dependent malate–aspartate shuttle.



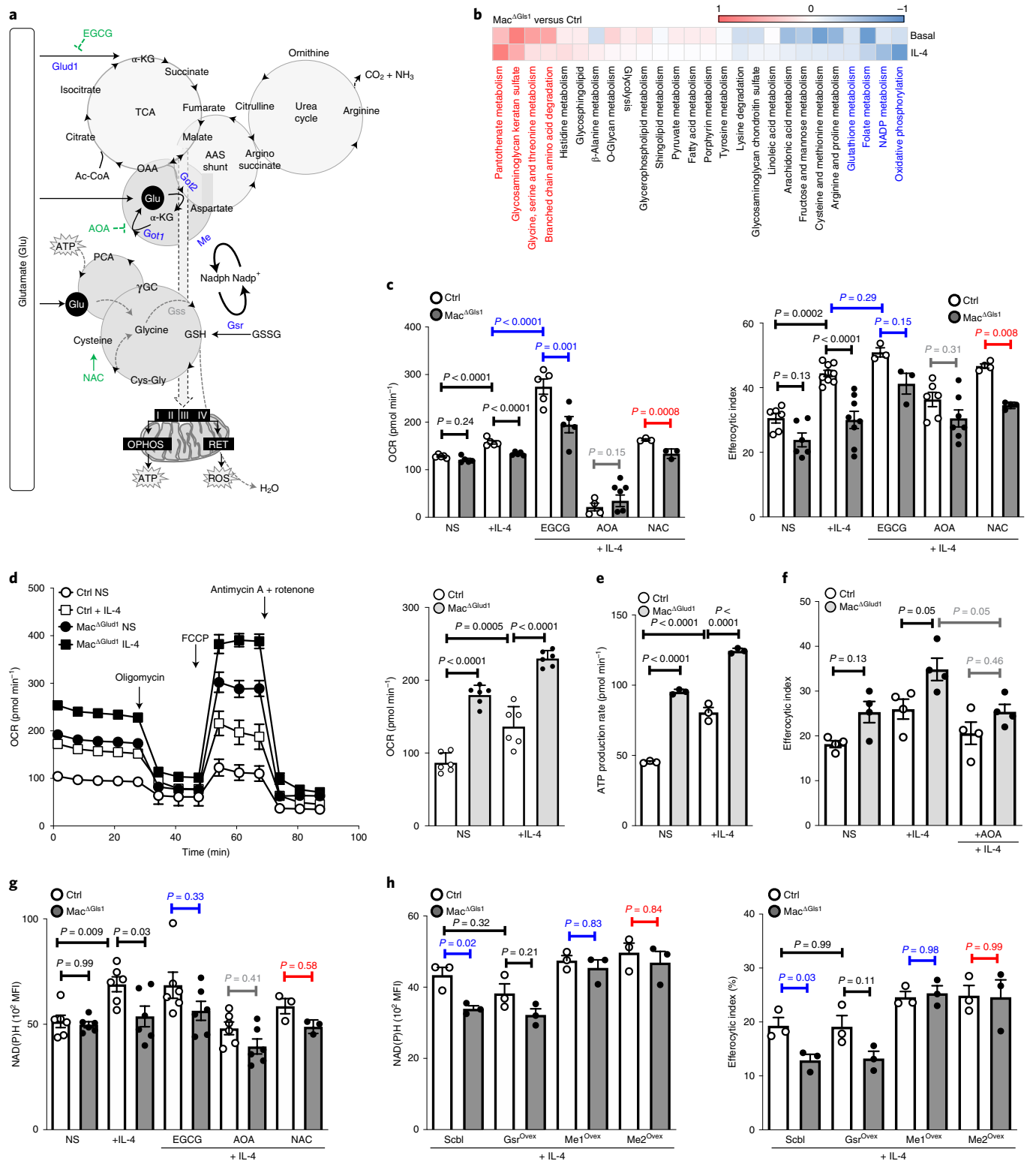


Fig. 4 | Non-canonical transaminase pathway allows glutaminolysis to fuel OxPHOS and support efferocytosis. a, Schematic representation of glutamate incorporation into metabolic cycles. Red indicates upregulated pathways; blue indicates downregulated pathways. **b**, Pathway-enrichment analysis of RNA-seq profiling in resting and reparative control or Mac^{ΔGls1} PCMs. Pathways highlighted in red and blue indicated significant up- or downregulation, respectively. **c**, OCR quantification (left) and efferocytic index (right) in control or Mac^{ΔGls1} BMDMs at steady state or after overnight IL-4 stimulation ± EGCG, AOA or NAC. **d–f**, OCR measurements (**d**) and ATP production rate (**e**) measured by Seahorse and efferocytic index (**f**) in control or Mac^{ΔGls1} BMDMs at steady state or after overnight IL-4 stimulation ± AOA. **g**, NAD(P)H levels as assessed by endogenous fluorescence in control or Mac^{ΔGls1} BMDMs at steady state or after overnight IL-4 stimulation ± EGCG, AOA or NAC. **h**, NAD(P)H levels (left) and efferocytic index (right) in reparative control or Mac^{ΔGls1} BMDMs after lentiviral vector-mediated overexpression of empty, glutathione disulfide reductase (*Gsr*) or MEs (*Me1* and *Me2*). All values are mean ± s.e.m. and are representative of at least one experiment ($n=5$ (**c**, left), $n=3$ to 12 (**c**, right), $n=6$ (**d**), $n=3$ (**e**h), $n=4$ (**f**), $n=6$ (**g**) of biologically independent replicates). *P* values were determined by ordinary one-way ANOVA with Tukey post hoc test for multiple comparisons (**c–h**). Each statistical bar color-coded represents an independent one-way ANOVA test against IL-4 conditions. Source data are provided as a Source Data file (**c–h**).

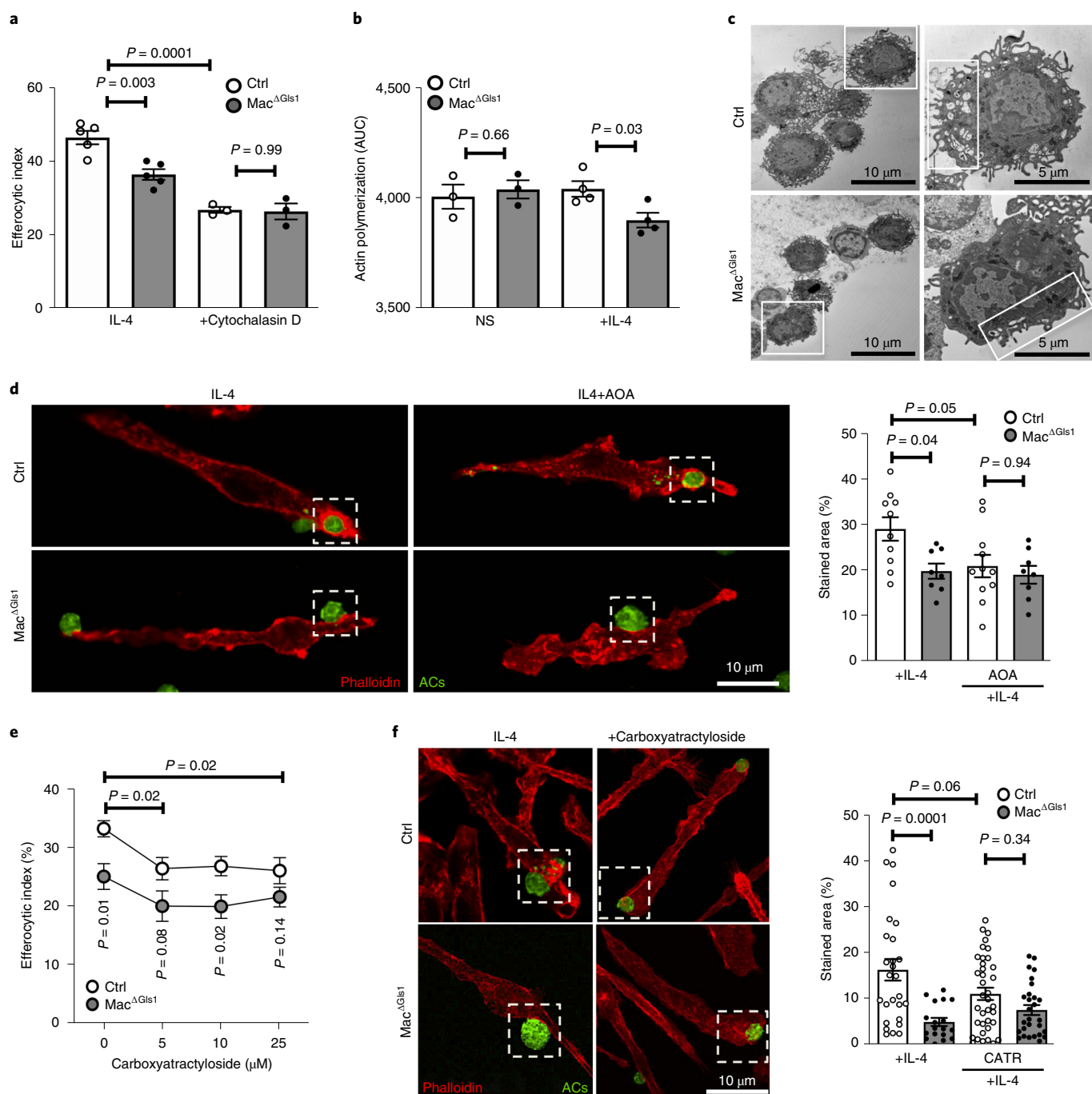


Fig. 5 | Glutamine metabolism supports the high-energy requirement of cytoskeletal rearrangement and corpse engulfment. **a**, Quantification of AC binding and internalization after treatment with 5 μ M cytochalasin D for 15 min before the addition of AC in control or Mac^{ΔGls1} BMDMs stimulated overnight \pm IL-4. **b**, Actin polymerization assay in resting and reparative control or Mac^{ΔGls1} BMDMs. **c**, Transmission electron microscopy imaging of control or Mac^{ΔGls1} PCMs. Scale bar, 10 μ m (left); scale bar, 5 μ m (right). **d**, Representative images of control or Mac^{ΔGls1} BMDMs stimulated overnight with IL-4 in the presence or absence of AOA and stained for F-actin (red) and ACs (green). Scale bar, 10 μ m. F-actin staining localized around the phagocytic cup was quantified. **e**, Efferocytic index in reparative control or Mac^{ΔGls1} BMDMs after treatment with the indicated concentrations of CATR for 15 min before the addition of AC. **f**, Representative images and quantification of F-actin staining localized around the phagocytic cup after treatment with 5 μ M CATR for 15 min before the addition of AC. All values are mean \pm s.e.m. and are representative of at least one experiment ($n = 3-5$ (**a**), $n = 3$ (**b**, **e**) of biologically independent replicates; $n = 9-11$ (**d**), $n = 18-39$ (**f**) of biologically independent measurements). *P* values were determined by ordinary two-tailed Student's *t*-test (**b**, **e**) or one-way ANOVA with Tukey post hoc test for multiple comparisons (**a**, **d**, **f**). Source data are provided as a Source Data file (**a**, **b**, **d**, **f**).

Glutaminolysis acts through AAS shunt to support efferocytosis. The non-canonical transaminase-dependent malate–aspartate shuttle is known to not only maximize production of ATP but also the number of NADPH molecules by being nested to the AAS

shunt⁷. Consistently, we also observed a decrease in NAD(P)H levels in reparative Mac^{ΔGls1} BMDMs that was recapitulated by GOT inhibition with AOA (Fig. 4g). To substantiate further these connections, we next measured the ratio between NADPH/NADP and

GSH (reduced glutathione)/GSSG (glutathione disulfide), known to scavenge ROS⁷. As expected, a decrease in the NADPH/NADP ratio was strongly correlated to the GSH/GSSG ratio in Mac^{ΔGls1} PCMs (Extended Data Fig. 5h) leading to higher ROS levels (Extended Data Fig. 5i). Supplementation with GSH to bypass this GSH salvage pathway defect raised basal OCR levels, ATP and NAD(P)H production and efferocytosis in reparative Mac^{ΔGls1} BMDMs almost to the levels of control macrophages (Extended Data Figs. 5j–l). In contrast, overexpression of glutathione disulfide reductase (GSR) did not increase but rather slightly attenuated NAD(P)H levels and had no impact on efferocytosis in reparative Mac^{ΔGls1} PCMs (Fig. 4h). Thus, we reasoned that impaired NADPH generation rather than NADPH consumption by GSH recycling was involved in the defective efferocytosis of *Gls1*-deficient macrophages. To validate this hypothesis, we overexpressed NADPH-producing malic enzymes (MEs) involved in the malate–pyruvate cycling pathway, nested to the non-canonical transaminase-dependent malate–aspartate shuttle (Fig. 4a). Overexpression of ME1 and ME2 using lentiviral particles not only restores the NAD(P)H levels in reparative Mac^{ΔGls1} PCMs but also their efferocytic capacity (Fig. 4h). Altogether, these findings pinpoint how glutaminolysis couples oxidative stress buffering to OxPHOS through non-canonical glutamine transamination metabolism.

Glutaminolysis controls apoptotic corpses engulfment. When compared to control PCMs, *Gls1*-deficient cells had similar transcriptional regulation of genes encoding proteins involved in the sensing of soluble mediators attracting the phagocytes to ACs ('smell' or 'find-me' signals), the direct contact and recognition of ACs by ligand–receptor interactions ('taste' or 'eat me' signals) and the corpse internalization and processing ('ingestion' and 'digestion' processes) (Extended Data Fig. 6a). Downregulation of various actin rearrangement/polymerization genes such as small GTPases Rac1 and Cdc42 or the newly identified Rac1 transcriptional regulator guanosine triphosphate (GTP)-exchange factor (GEF) Dbl has recently been linked to metabolic adaptation during continual efferocytosis^{4,10}. Although a slight downregulation of *Cdc42* mRNA expression was observed in reparative *Gls1*-deficient macrophages, this was not observed for Rac1 (Extended Data Fig. 6b) and Dbl expression (Extended Data Fig. 6c). In contrast, some nucleotide metabolism enzymes such as *Nme1*, *Nme6* or *Suclg1*, known to encode enzymes modulating GEF activity through spatiotemporally controlled GTP production, were downregulated in *Gls1*-deficient macrophages (Extended Data Fig. 6d). Nevertheless, overexpression of these enzymes had little effect on efferocytosis (Extended Data Fig. 6e). Thus, we reasoned that glutaminolysis must control the efferocytic response through post-transcriptional regulation. Treatment of *Gls1*-deficient macrophages for 15 min with cytochalasin D, an actin polymerization inhibitor, indicated that the decrease in AC efferocytosis in Mac^{ΔGls1} BMDMs was due to a defect in AC internalization (Fig. 5a). These findings suggest a post-transcriptional defect in the dynamic rearrangement of actin to engulf corpse during phagosome sealing⁶. This is an energy-intensive process, as actin polymerization and depolymerization steps require an ATP-dependent nucleation phase of new actin filaments (Extended Data Fig. 6b) and this process is regulated by RAC1 and CDC42 activities²¹. We indeed observed a slower polarization of G- to F-actin in reparative Mac^{ΔGls1} macrophages (Fig. 5b) along with reduced activity of CDC42 and a trend for RAC1 (Extended Data Fig. 6f,g). Consistently, transmission electron microscopy revealed less membrane ruffling surrounding the Mac^{ΔGls1} BMDMs (Fig. 5c). Phalloidin immunostaining, 10 min after efferocytosis, also revealed a general decrease in the amount of F-actin staining at the leading edge of membrane ruffle formation surrounding the ACs, indicative of reduced actin polymerization in efferocytic Mac^{ΔGls1} phagocytes (Fig. 5d). Blocking the energy-intensive actin rearrangement with

NSC-23766, a RAC1 inhibitor or ML141, a CDC42 inhibitor recapitulated the efferocytic defect observed in reparative and resolving Mac^{ΔGls1} macrophages (Extended Data Fig. 6h,i). This effect seems independent of the post-transcriptional regulation of RAC1 by the Drp1-mediated mitochondrial fission³, as reduced efferocytosis in Mac^{ΔGls1} BMDMs was still observed after Drp1 inhibition with MDIVI-1 treatment (Extended Data Fig. 6h,i). In contrast, we validated the role of non-canonical glutamine transamination pathway in the energy-intensive engulfment process by blocking the AAS shunt with AOA, which blunted RAC1 and CDC42 activities (Extended Data Fig. 6f,g) and reduced F-actin immunostaining to the same level after AC engulfment in reparative control and Mac^{ΔGls1} BMDMs (Fig. 5d). Finally, to link the defect in mitochondrial ATP generation to the high-energy requirement of cytoskeletal rearrangements in reparative Mac^{ΔGls1} macrophages, we blocked the transport of ATP produced from OxPHOS to the cytoplasm by targeting the mitochondrial carrier adenine nucleotide translocator (ANT) with the carboxyatractyloside (CATR) inhibitor. A 15-min treatment with this inhibitor was sufficient to dose dependently reduce efferocytosis in control macrophages with minimal impact on reparative Mac^{ΔGls1} BMDMs abolishing the difference between genotypes at the highest concentration (Fig. 5e). Consistently, ANT inhibition for 15 min with CATR limited the amount of F-actin staining around the phagocytic cup in control macrophages almost to the levels of reparative Mac^{ΔGls1} BMDMs (Fig. 5f). Thus, our results reveal that glutaminolysis and non-canonical transaminase pathways are essential to maximize the number of ATP molecules produced in mitochondria and meet the demand for high-energy actin polymerization that facilitates the process of corpse engulfment (Extended Data Fig. 7).

Discussion

Macrophages require substantial amount of nutrients after ingestion of ACs (efferocytosis) to maintain normal tissue function⁶. We and others have demonstrated that efferocytes can adapt their metabolism to face cholesterol and fatty acid overload during this process^{11,22–24}. Increased glucose uptake preceding AC engulfment could also prime continued AC clearance¹⁰. We now uncover that GLS1-dependent glutaminolysis is required to optimize AC clearance upon IL-4 stimulation or continued AC uptake by efficiently reprogramming macrophage metabolism. Indeed, conversion of glutamine through non-canonical transaminase pathways couples oxidative stress buffering to ATP production to meet the demand for high-energy actin dynamics and cytoskeletal rearrangements.

Glutamine is considered a conditionally essential amino acid because of its role during metabolic stress, including injury^{7,8} and predicted macrophage activation profiles in aortas of atherosclerotic mouse models²⁵. However, the fundamental link between GLS1 and efferocytosis in this setting remains to be elucidated. Strikingly, despite enhanced glutamine utilization in the aortas of atherosclerotic mice, we observed impaired glutamate conversion and reduced *Gls1* expression, reflecting perturbed glutaminolysis. In our mouse and human datasets, we also observed that *Gls1* expression within plaques was positively associated to canonical alternative polarization markers suggesting that glutaminolysis, rather than glutamine uptake could predict macrophage polarization. *Gls1* expression also negatively correlated with necrotic cores.

Modulation of glutamine metabolism can lead to strikingly different phenotypes in immune cells. For instance, it has recently been suggested that glutaminolysis could promote mTORC1 signaling during type 1 helper T cell differentiation²⁶. In the current setting, we did not observe perturbations of glycolysis or downstream mTOR signaling pathways in glutaminolysis deficient macrophages. Because an enhanced transcriptomic signature of genes involved in amino acid catabolism in *Gls1*-deficient cells was observed, we investigated the metabolism of specific amino acids that has recently

emerged to control macrophage effector functions. For example, BC-AAAs cause itaconate accumulation, a hallmark of macrophage proinflammatory response^{27,28}. The group led by Tabas et al. have also recently reported that the metabolism of AC-derived arginine or ornithine to putrescine is required for continual efferocytosis by a mechanism involving cytoskeletal rearrangements⁴ and potentially linked to mitochondrial fission³. However, impaired macrophage glutaminolysis likely occurs independently of the aforementioned amino acid pathways, as similar levels of BC-AAAs and putrescine were observed in *Gls1*-deficient macrophages. Furthermore, inhibition of BCAT or ornithine supplementation did not rescue the defective efferocytosis of these cells. Thus, *Gls1*-deficient cells may impact amino acid catabolism as an attempt to compensate for the loss of glutamate generation, but this was unlikely the cause of the defective efferocytosis in these cells.

Glutamine can be converted through GLUD1 or non-canonically into GSH synthesis or via transaminases. Canonical glutaminolysis could support α -KG generation to orchestrate the jumonji domain containing-3 (Jmjd3, KDM6B)-dependent epigenetic reprogramming of alternatively activated macrophages²⁹. However, we did not observe perturbations of α -KG-dependent epigenetic activity and α -KG supplementation did not rescue the defective efferocytosis observed in *Gls1*-deficient macrophages. Unexpectedly, *Glud1* deficiency also exhibited an opposite efferocytosis phenotype relative to *Gls1* deficiency suggesting that the reduced glutamate generated in *Gls1*-deficient macrophages impacted non-canonical glutaminolysis pathways. Consistently, high-throughput transcriptional and metabolic profiling indicated that defective glutaminolysis in macrophages predominantly perturbed downstream non-canonical GSH synthesis and transaminase pathways. Mechanistic studies further confirmed that glutaminolysis was essential to limit oxidant stress but also to support mitochondrial OxPHOS and ATP production in resolving and reparative macrophages.

The perturbation of non-canonical GSH synthesis in macrophages with defective glutaminolysis may have pleiotropic effects. First, it could impact mitochondrial redox status that has been previously shown to metabolically program macrophage effector functions^{16,17}. However, we excluded a causal role of mitochondrial ROS in the metabolic reprogramming and defective efferocytosis of *Gls1*-deficient macrophages. It has been previously suggested that glutamate oxidation by complex I can be used to direct the electron transport chain (ETC) in the forward direction independently of the redox state of CoQ and $\Delta\Psi_m$ ^{30,31}. Thus, the enhanced mitochondrial ROS production in *Gls1*-deficient macrophages is unlikely the consequence of the perturbed non-canonical GSH synthesis in these cells but rather a 'by-products' of the defective OxPHOS and ATP generation and is not responsible for their defective efferocytosis. A second scenario involved ATP leakage through the γ -glutamyl futile cycle synthesis, which is part of non-canonical GSH synthesis pathway⁷. However, we also excluded a perturbation of this pathway in *Gls1*-deficient macrophages. Finally, the lower GSH/GSSG ratio that was associated with a higher oxidant stress in macrophages with defective glutaminolysis rather suggested perturbation in the recycling of GSH to GSSG, which depends on NADPH-consuming or producing enzymes. Although GSH supplementation rescued the defective efferocytosis of *Gls1*-deficient macrophages, overexpression of GSR, the rate-limiting enzyme of GSH recycling that consumes NADPH, did not. Further studies will be required to pinpoint whether the beneficial effect of GSH in reparative *Gls1*-deficient macrophages involves enhanced respiratory chain efficiency by limiting CoQ oxidation and subsequent mitochondrial supercomplex assembly^{32,33} or reduced NADPH consumption, which 'energy value' can be roughly estimated at between 2.5 and 3.5 ATP equivalents for purposes of comparing energy inputs and outputs of metabolic pathways³⁴. Nevertheless, the mechanism by which GSH rescued

efferocytosis in *Gls1*-deficient macrophages was associated with its ability to improve OxPHOS, ATP generation and NAD(P)H levels.

The transaminase-dependent malate–aspartate shuttle is nested to the AAS shunt and requires glutamate to regenerate NADH, which is used to transfer electrons to the ETC. This is required to maximize the number of ATP molecules produced in mitochondria and favor NADPH production through ME-dependent malate–pyruvate cycling pathway to support GSH salvage pathway⁷. Consistently, all markers of these pathways were downregulated in *Gls1*-deficient macrophages along with reduced activity of mitochondrial complex I and II. The central role of ATP produced within mitochondria after glutamate is channeled into the malate–aspartate shuttle by GOT-dependent transamination in efferocytes was ultimately highlighted by directly targeting GOTs and mitochondrial complex II and III. Finally, overexpression of ME1 and ME2 not only restored NAD(P)H levels but also the defective efferocytic capacity of reparative *Gls1*-deficient macrophages. Thus, defective non-canonical transaminase pathway in *Gls1*-deficient macrophages reveals how glutaminolysis couples oxidative stress buffering to OxPHOS and ATP production, which is linked to the ability of these pathways to power cells with the reducing equivalents necessary to detoxify ROS and support the TCA cycle anapleurosis required for efficient efferocytosis.

The high-energy demand for cytoskeletal rearrangements during efferocytosis has previously been suggested, but the underlying mechanisms remain poorly understood². Actin remodeling is an energy-intensive process involving polymerization and depolymerization steps and formation of membrane ruffling for AC recognition and internalization that can be metabolically regulated by transcriptional^{4,10} or post-transcriptional modifications^{3,24}. However, we did not identify a specific genetic signature that could link glutaminolysis to efferocytosis including the one targeting Rac1 and Cdc42, which are key regulators of this process. For instance, we did not observe a role for the recently identified transcriptional regulation of Rac1 by GEF Dbl¹. Thus, defective efferocytosis and actin remodeling was rather the consequence of post-transcriptional regulation in macrophage with defective glutaminolysis. Along with reduced ATP production in *Gls1*-deficient macrophages, we indeed observed impaired actin polymerization and reduced Cdc42 and Rac1 activities. This was ultimately associated with defective F-actin polymerization in membrane ruffles after the ingestion of ACs that was recapitulated by targeting the non-canonical transaminase pathway. This process required the ANT-dependent transport of ATP from mitochondria through the cytoplasm. Thus, several complementary mechanisms exist to sustain an efficient successive clearance of ACs. We now identified that macrophage glutaminolysis supports the high-energy demand for F-actin remodeling during this process.

Collectively, our results reveal a dependence on transaminases for metabolism of the glutamine carbon skeleton during key macrophage effector functions that are required for tissue repair. Mechanistically, these reactions orchestrate ATP generation through the ETC in the presence of IL-4 or during continued AC clearance. These findings support the larger concept that any process that compromises the metabolic reprogramming and ATP production of efferocytes will likely result in dire pathologic consequences. Conversely, therapeutic interventions to enhance macrophage glutaminolysis and boost efferocytosis have the potential to subvert maladaptive inflammation and tissue necrosis.

Methods

Human atherosclerosis. Tissue collection was part of the Maastricht Pathology Tissue Collection and further storage and use of the tissue was in line with the Dutch Code for Proper Secondary use of Human Tissue and the local Medical Ethical Committee (protocol number 16-4-181).

Carotid arteries were collected from 22 symptomatic male patients undergoing carotid endarterectomy in the Maastricht Human Plaque Study (72.9 \pm 6.3 years

old) as previously described³⁵. Formalin-fixed, paraffin embedded 5-mm segments were alternated with frozen segments for RNA isolation. Two independent pathologists then classified the segments in a blind fashion as fibrous cap atheroma with or without intraplaque hemorrhage (16 stable segments and 27 unstable segments, respectively) according to H&E staining. Stable and unstable snap-frozen segments were used for further microarray analysis. Snap-frozen segments were pulverized and 5–20 mg of material was subjected for transcriptomics. RNA isolation was performed by guanidium thiocyanate extraction and further purified with the Nucleospin RNA II kit (Macherey–Nage). RNA quality and integrity were determined using the Agilent 2100 Bioanalyzer. Biotinylated cRNA was prepared with Illumina TotalPrep RNA Amplification kit (Ambion) and 750 ng cRNA per sample was used for hybridization (Illumina Human Sentrix-8 v.2.0, Beadchip). Scanning was performed on the Illumina Beadstation 500 (Illumina) and image analysis was conducted using the Illumina Beadstudio v.3 gene expression software. A total of 22,184 human transcripts were analyzed in the R Bioconductor lumi package. First, a variance stabilizing transformation, which is incorporated in the lumi package, was performed. Second, the Robust Spline Normalization algorithm in the lumi package was applied to normalize the data. Differential gene expression analysis was performed by using the function *lmFit()* provided in Limma R package on preprocessed transcriptomics data.

The 88 adjacent tissue sections were phenotyped extensively for plaque size, necrosis, inflammation (CD68, CD3, arginase, iNOS), SMCs (α SMA), collagen (Sirius red) and angiogenesis (CD31⁺ microvessel density, newly formed CD105⁺ microvessels, α SMA⁺ mature microvessels, Lyve⁺ lymphatic density). Pearson correlation analysis was performed to assess the association between gene expression and plaque phenotypic traits.

Mice. Gls1^{fl/fl} mice were kindly provided by S. Rayport (Glstm2.1Sray/J) deposited at The Jackson Laboratory) and were crossed with *Lyz2*^{Cre} mice (B6.129P2-Lyz2tm1(cre)lfo/J, The Jackson Laboratory) or *Mx1*^{Cre} mice (B6.Cg-Tg(Mx1-cre)1Cgn/J) on an ApoE-deficient genetic background (B6.129P2-ApoEtm1Unc/J). *Mx1*^{Cre} mice (B6.Cg-Tg(Mx1-cre)1Cgn/J) were also crossed with C57BL/6 Glud1 floxed mice (kindly provided by P. Maechler). For each experiment, co-housed littermate male and female controls were used between 8–14 weeks of age. Animal protocols were approved by the Institutional Animal Care and Use Committee of the French Ministry of Higher Education and Research and the Mediterranean Center of Molecular Medicine (Inserm U1065) and were undertaken in accordance with the European Guidelines for Care and Use of Experimental Animals. Animals had free access to food (chow diet A04, Safe) and water and were housed in a controlled environment with a 12-h light–dark cycle, constant temperature (21.7–22.8 °C) and relative humidity (50–60%). Water and cages were autoclaved. Cages were changed once weekly and the health status of the mice was monitored using a dirty bedding sentinel program. Hyperlipidemia was induced by feeding the mice with a WD (TD88137, Sniff) for 12 weeks.

Poly(I:C) induction. *Mx1*^{Cre} mice were intraperitoneally injected with 1 mg ml⁻¹ poly(I:C) three times every 2 d. Mice were used for experimentation 3 weeks later.

IL-4c in vivo treatment. Mice were intraperitoneally injected with IL-4 complexed to anti-IL-4 monoclonal antibody (IL-4c; containing 5 μ g of IL-4, PeproTech and 25 μ g of anti-IL-4 clone 11B11, BioXcell). After 36 h, PCMs were collected and analyzed by flow cytometry.

Cell culture, PCMs and BMDMs generation. BM cells were collected from mouse femur and tibia and differentiated in the presence of recombinant mouse M-CSF (20 ng ml⁻¹; Miltenyi) in complete RPMI 1640 medium (Corning) containing 10 mM glucose, 2 mM L-glutamine, 100 U ml⁻¹ of penicillin/streptomycin and 10% FBS for 7 d at 37 °C and 5% CO₂. PCMs were obtained by peritoneal lavage with 5 ml of PBS.

Cell treatments. At day 7, BMDMs were collected, plated and activated overnight as indicated. Peritoneal cells were obtained by peritoneal lavage with 5 ml of PBS. Cells were plated and cultured overnight in complete RPMI 1640 medium (Corning) containing 10 mM glucose, 2 mM L-glutamine, 100 U ml⁻¹ penicillin/streptomycin and 10% FBS at 37 °C and 5% CO₂. Cell were incubated overnight with the following treatments: IL-4 (20 ng ml⁻¹, Peprotech), AOA (200 μ M, Sigma), dimethyl- α -KG (1 mM, Sigma), EGCG (100 μ M, Sigma), GSH (10 mM, Sigma), L-ornithine (1 mM, Sigma), BCATc inhibitor (20 μ M, Cayman Chemical), gabapentin (10 μ g ml⁻¹, Sigma), 3NPA (1.68 mM, Sigma), antimycin A (0.1 μ M, Sigma), Tempol (4 mM, EMD Millipore), mitoquinol (200 nM, Cayman Chemical), NAC (10 mM, Sigma), MDIVI-1 (10 μ M, Sigma), NSC-23766 (50 μ M, EMD Millipore) or ML141 (10 μ M, EMD Millipore) (Supplementary Table 2).

siRNA transfection. Cells were transfected with Got1/Got2 short-interfering (si) RNA (L-043492-01-0005 and L-043495-01-0005, Dharmacon) or control siRNA (D-001810-01-05, Dharmacon) (referred to as Scbl) at 30 nM using Lipofectamine RNAiMAX (Life Technologies), according to the manufacturer's instructions.

Lentivirus overexpression. Cells were spin-transfected for 90 min at 1,300g with Gls1, lentivirus (LVM(VB200119-1197bpb)-C, Vectorbuilder), Nme1 (vector ID: VB200120-1064ucb, Vectorbuilder), Nme6 (vector ID: VB200120-1213tjc, Vectorbuilder), Suclg1 (vector ID: VB200120-1214hxx, Vectorbuilder), Me1 (vector ID: VB201125-1076tsb, Vectorbuilder), Me2 (vector ID: VB201125-1253dre, Vectorbuilder), Gsr (vector ID: VB201125-1094mzr, Vectorbuilder) or control lentivirus (LVM(VB200120-1215tyv)-C, Vectorbuilder) (referred to as Scbl) and used at a multiplicity of infection (MOI) of 10. The same protocol was used for AOX overexpression using Lenti-ONE AOX viral particles (GEG Tech) and Lenti-ONE gfp (referred to as empty) viral particles (GEG Tech) at an MOI of 5. After 6 h, cells were washed and the medium was replaced with fresh medium for 48 h before treatment.

Western blotting. Large peritoneal macrophages were cell-sorted and then lysed in RIPA buffer containing protease inhibitors cocktail (Thermo Fisher) and agitated for 1 h at 4 °C before centrifugation at 20,000g for 10 min at 4 °C. Protein samples were resolved on 10% SDS-PAGE gels and were then transferred onto polyvinylidene difluoride membrane using a wet transfer system. Membranes were blocked in 5% (w/v) BSA in Tris-buffered saline-Tween for 1 h at room temperature. Membranes were then incubated with primary antibody (anti-Glud1 or anti-Gls1 antibodies (Abcam)) followed by the appropriate horseradish peroxidase-conjugated secondary antibody. Anti- α -actin monoclonal antibody (Santa Cruz) was used as loading control. Proteins were detected by substrate horseradish peroxidase (Sigma). Antibody validations were performed by suppliers and antibodies were used according to manufacturer's instructions.

Analysis of atherosclerotic plaque. Mice were killed and slowly perfused with 10 ml of ice-cold PBS. The hearts and aortas were carefully excised and fixed in 4% paraformaldehyde containing 30% sucrose. The aortas were stained with Oil Red O (Sigma, O0625) to evaluate plaque neutral lipid content. The hearts were embedded in OCT compound (Gentaur) and stored at -80 °C before analysis. Then, 10- μ m cryosections of the aortic sinus were prepared. Oil Red O staining was used to detect neutral lipid content in the plaque combined with H&E staining to analyze tissue architecture. Plaque macrophages were visualized using purified anti-CD68 monoclonal antibody (clone FA-11, AbD Serotec). Anti-rat Alexa Fluor 488-conjugated antibody (A-11006, Life Technologies) was used for detection of CD68 staining. For analysis of plaque macrophage proliferation, anti-Ki67 PE conjugated monoclonal antibody (clone 16A8, BioLegend) was used. Nuclei were revealed with DAPI counterstaining (2 μ g ml⁻¹). TUNEL staining was performed using the DeadEnd Fluorometric TUNEL System (Promega). Plaque area quantification were measured with ImageJ software.

Echography. Male mice were fully anesthetized with 1.5% isoflurane before and during ultrasound scanning. Before all ultrasound scanning, the hair of the mouse chest wall was carefully removed and warm ultrasound transmission gel was liberally applied to ensure optimal image quality. Echocardiography was performed using a high-frequency Vevo2100 (Visualsonics)-imaging.

Transmission electronic microscopy. Cells were observed with transmission electron microscopy for ultrastructural analysis. Cells were fixed in a 1.6% glutaraldehyde solution in 0.1 M sodium phosphate buffer at room temperature and stored overnight at 4 °C. After rinsing three times in 0.1 M cacodylate buffer (15 min each), cells were post-fixed in a 1% osmium tetroxide and 1% potassium ferrocyanide solution in 0.1 M cacodylate buffer for 1 h at room temperature. Cells were subsequently dehydrated in a series of acetone baths (90%, 100% three times, 15 min each) and progressively embedded in Epon 812 resin (acetone/resin 1:1, 100% resin twice, 2 h for each bath). Resin blocs were finally left to harden in a 60 °C oven for 2 d. Ultrathin sections (70 nm) were obtained with a Reichert Ultracut S ultramicrotome equipped with a Drukker International diamond knife and collected on 200 mesh copper grids. Sections were stained with lead citrate and uranyl acetate. Transmission electron microscopy observations were performed with a JEOL JEM-1400 transmission electron microscope, equipped with a Morada camera at a 100-kV acceleration voltage.

In vitro efferocytosis analysis. BMDMs and PCMs were generated and stimulated as described above. To generate ACs, thymii from C57BL/6J mice were collected and mechanically dissociated, filtered on 100- μ m nylons (Falcon), pelleted and resuspended in RPMI medium supplemented with 10% FBS. Apoptosis was induced by UV exposure at 312 nm for 10 min and cells were maintained in culture for an additional 2 h. This method results in 70–90% apoptosis²³. ACs were labeled with CellTrace Violet Cell Proliferation kit (Thermo Fisher) according to the manufacturer's instructions. Fluorescent ACs were washed twice with PBS before use. For one round efferocytosis: stained ACs were added at a 5:1 ratio on plated macrophages for 45 min. For two rounds efferocytosis: unlabeled ACs were added at a 5:1 ratio on plated macrophages for 45 min. Cells were then washed three times and macrophages were incubated for 1 h. Stained ACs were then added at a 5:1 ratio on macrophages for 45 min. Cells were washed three times and macrophages were stained and analyzed for AC content and activation markers by flow cytometry. In some experiment, macrophages were treated for 15 min before

efferocytosis with cytochalasin D (5 μ M, Sigma). For Seahorse extracellular flux analysis ACs were injected directly, before drug treatment, during the assay.

Escherichia coli phagocytosis assay. BMDMs were loaded with 1 μ g of fluorescein-labeled *E. coli* K12 Bioparticles (Thermo Fisher) for 30 min at 37 °C and intracellular fluorescence of engulfed particles was calculated after quenching of the extracellular probe by trypan blue according to the manufacturer's instruction.

Immunofluorescence. BMDMs and ACs were generated and stimulated as described above. ACs were stained with CellTrace CFSE (Invitrogen) for 30 min before one round efferocytosis. After 15 min of efferocytosis, BMDMs were washed with a 37 °C heated medium and fixed for 10 min at 37 °C with 4% PFA culture medium. Cells were then saturated for 30 min in PBS 10% FBS. Cells were incubated for 30 min with Texas Red-X Phalloidin (Invitrogen). Cells were then washed thoroughly and coverslips were mounted with aqueous glue. Sections were observed the following day by fluorescent microscopy.

In vivo efferocytosis analysis. ACs were generated as described above. Mice were i.v. injected with 2×10^7 stained ACs and 1 h later, the spleen and liver were collected and analyzed by flow cytometry.

In vitro flow cytometry analysis. Cells were stained for 25 min at 4 °C protected from light. For flow cytometry analysis the following list of antibodies was used: MitoSOX Red (Thermo Fisher), ROS (Thermo Fisher, CM-H2DCFDA), CD206 PerCp-Cy5.5 conjugated (clone C068C2, BioLegend), MerTK PE conjugated (clone 2B10C42, BioLegend), CD115 PE conjugated (clone AFS98, eBioscience), CD64 Brilliant Violet 421 conjugated (clone X54-5/7.1, BioLegend), F4/80 Pe-Cy7 conjugated (clone BM8, BioLegend), annexin V (BioLegend). Antibody validations were performed by suppliers and antibodies were used according to manufacturer's instructions. Cells were then washed, centrifuged and data were acquired on BDFACSCanto flow cytometer. FSC/SSC gating was used to exclude dead cells and debris followed by FSCA/FSCB to select singlets. Gating strategy for all viable cells have been described in the manuscript. Data collection was performed using FACS DIVA software and analysis was performed using FlowJo software (TreeStar).

Intracellular flow cytometry. For all intracellular staining: phospho-S6 ribosomal protein (Ser235/236) PE conjugated (clone D57.2.2E, Cell Signaling), c-Myc PE Conjugate (Clone D84C12, Cell Signaling). Cells were removed from medium, stained for surface, fixed, then stained for intracellular proteins using Foxp3 Transcription Factor Fixation/Permeabilization kit (BD Biosciences).

In vivo flow cytometry analysis. Cells were collected from spleen, peritoneal cavity, BM, liver and brain. Tissues were collected after cardiac PBS perfusion. Splenocytes were extracted by pressing spleens through a stainless-steel grid. Peritoneal and BM leukocytes were collected by PBS lavage. Livers and brains were cut into small pieces and digested for 30 min with HBSS medium containing 1.5 mg ml⁻¹ collagenase D (Roche) at 37 °C. For liver and microglia preparation, an additional purification step was performed by Percoll gradient. Single-cell suspension was submitted to red blood cell lysis, filtration and centrifugation for 5 min at 400g. Cell suspensions were stained with the appropriate antibodies for 30 min on ice protected from light. The following antibodies were used for macrophage flow cytometric analysis: CD11b Brilliant Violet 510 conjugated (clone M1/70, BioLegend), CD115 PE conjugated (clone AFS98, eBioscience), CD45 APC-Cy7 conjugated (clone 30-F11, BD Biosciences), CD64 Brilliant Violet 421 conjugated (clone X54-5/7.1, BioLegend), CD11c APC conjugated (clone N418, BioLegend), F4/80 Pe-Cy7 conjugated (clone BM8, BioLegend), CD206 PerCp-Cy5.5 conjugated (clone C068C2, BioLegend) and CD301 FITC conjugated (clone ER-MP23, Bio-Rad). Cells were then washed, centrifuged and data were acquired on a BDFACSCanto flow cytometer. NAD(P)H levels were assessed by endogenous fluorescence emission within the 420–480 nm range. Data collection was performed using FACS DIVA software and analysis was performed using FlowJo software (TreeStar) as described above.

Seahorse extracellular flux analysis. For the extracellular flux assay, 1×10^5 BMDMs or large peritoneal macrophages were plated in a Seahorse Bioscience culture plate. Cells were then incubated overnight with different drugs and metabolites. OCR and ECAR was measured by an XF96 Seahorse Extracellular Flux Analyzer following the manufacturer's instruction. In the Seahorse assay, cells were treated with oligomycin (1 μ M), FCCP (1.5 μ M), rotenone (1 μ M) and antimycin A (0.1 μ M). ATP production is measured after injection of oligomycin and calculated using the Seahorse XF report generator. Each condition was performed in three replicates.

RNA-seq. PCMs were obtained by lavage as described above. Then cells were stained with CD64 Brilliant Violet 421 conjugated (clone X54-5/7.1), ICAM-2 Alexa Fluor 647 conjugated (clone 3C4(MIC2/4)) and CD115 PE conjugated (clone AFS98). These antibodies allow us to separate the two subsets of peritoneal macrophages with only the major one expressing ICAM-2 (ref. ³⁶). Cells were sorted on BD FACS Aria flow cytometer. Total RNA was extracted with an RNeasy

Mini kit (QIAGEN) according to the manufacturer's protocol and quality was assessed by Nanodrop (Ozyme). Library constructions were conducted as described previously⁹. Libraries were sequenced at the Center for Applied Genomics (SickKids) using a HiSeq 2500 (Illumina).

Integrated network analyses. Network-based integration of metabolite and gene expression datasets was conducted using Shiny Gam as previously described⁹. We also developed DreamBio, a complementary topological tool for Integrated Network Analysis mapped into KEGG pathway. The same strategy than Shiny Gam was used⁹ (<https://artyomovlab.wustl.edu/shiny/gam/>), except that GEPHI GEXF (graph exchange format) was converted from KGML to be analyzed through Sigma library, which is dedicated to graph drawing. Up- and downregulated metabolic genes based on *P* values calculated with Phantasus⁹, were mapped into models maintaining all essential KEGG pathway attributes. DreamBio will soon become freely available at <https://biotest.hematometabolism.science/>.

Fluxomics. Metabolite extraction of BMDMs was performed on 2.5 million cells per well using 70 °C aqueous 70% ethanol as described previously³⁷. Briefly, [¹³C]-glutamine (1 mM) was added on free-glutamine medium cells for 4 h. At collection, cells were placed immediately on ice, the medium was removed and cells were washed three times with ice-cold PBS to remove residual medium. Intracellular metabolites were extracted twice with hot ethanol. For LC–MS, samples were dried under nitrogen flow and reconstituted in a milliQ water/acetonitrile (1:1) mixture for injection using a UPLC Acquity (Waters) separation system coupled with a Xevo G2 ToF (Waters). Compounds were ionized using an electrospray ionization source in negative mode. Data processing was performed in MATLAB (Mathworks) using a custom-made in-house protocol. Compound identification was performed using both retention time of authentic standards and accurate mass with an accepted deviation of 0.005 Da. Raw data was converted to netCDF format using Chemstation (Agilent), before processing in MATLAB R2014b (Mathworks) using PARADISE software. All MS sample processing and analyses were performed by MS-Omics.

Metabolomics. Metabolomics analyses were performed at CriBioM as previously described³⁸. Briefly, control and Gls1-deficient BMDMs were treated with or without 20 ng ml⁻¹ IL-4 as indicated in the figure legends. Metabolites were extracted by exposing cells to cold methanol and analyzed by LC–MS.

Typhoon Biomolecular Imager. A total of 2 μ Ci of [¹⁴C]-labeled glutamine were i.v. injected and mice were killed 15 min later. Aortas were collected and the associated adipose tissue was carefully dissected and removed. Imaging for [¹⁴C]-labeled glutamine was performed on a Typhoon Biomolecular Imager (Amersham). Whole-mount staining with Oil Red O paralleled this analysis on the same samples.

Thin-layer chromatography. Aortic tissues were homogenized with 5% HClO₄ solution and the radioactivity incorporated in this extract was measured before being dropped on silica-gel POLYGRAM pre-coated TLC sheets (Sigma). Separation of ¹⁴C glutamine and the ¹⁴C glutamine-derived glutamate was achieved in hexane/diethyl ether/formic acid (80:20:1 v/v/v) running buffer. The radioactivity was quantified and expressed as a percentage of ingested radioactivity.

[³H]-Thymidine incorporation. BMDMs were generated and stimulated as described above. The day before the experiment, cells were stimulated overnight with IL-4 (20 ng ml⁻¹). [³H]-Thymidine (1 μ Ci) was added on cells in regular media for 2 h. Cells were collected, centrifuged, washed with PBS and resuspended in NaOH (0.1 N)/SDS (0.1%) before adding scintillation.

Plasma cholesterol and triglyceride content. Plasma cholesterol and triglyceride content were measured with LabAssay Cholesterol (Sobioda) and Triglycerides Reagent (Diasys) according to the manufacturer's protocol.

Glutamine/glutamate and GSH/GSSG measurements. Commercially available kits Glutamine/Glutamate-Glo Assay (Promega) and GSH/GSSG-Glo Assay (Promega) were used in accordance with the manufacturer's instructions.

Complex I/II activity assay. Enzyme Activity Assay kit (ab109721 and ab109908) was determined according to the manufacturer's instruction.

Rac1 and Cdc42 activity assay. Rac1 G-LISA Activation Assay kit (Cytoskeleton BK128) and Cdc42 G-LISA Activation Assay kit (Cytoskeleton BK127) was used according to the manufacturer's instructions.

G-actin/F-actin assay. G-Actin/F-Actin activity was determined with G-Actin/F-Actin In Vivo Assay Biochem kit (Cytoskeleton) according to the manufacturer's instructions.

Actin polymerization assay. Actin polarization activity was determined with Actin Polymerization Biochem kit (Cytoskeleton) according to the manufacturer's instructions.

KDM6 and Tet2 activity assay. Tet2 and KDM6 activities were determined with MethylFlash Global DNA Hydroxymethylation (5-hmC) ELISA Easy kit (Epigentek) and KDM6A/KDM6B Activity Quantification Assay kit (Abcam), respectively according to the manufacturer's instructions.

IL-10 secretion. IL-10 concentration in supernatant was measured using Mouse IL-10 Duoset ELISA kit (R&D) according to the manufacturer's instructions.

Real-time qPCR. Total RNA was isolated and complementary DNA was synthesized for real-time qPCR analysis. Gls1 (F: GCACATTATTCACCCGGTAACC, R: CTGCCACCCACCATCC), Mertk (F: AAAGGTCCCGTCTGTCT, R: CCATCAAAACCAGGGACCC), Timd4 (F: AAAGGTCCCGCTTCACTAC, R: TGCTTCTTTGAGAGTGATTGGA) Gas6 (F: CGGCGCTACCAAGTCTTC, R: CGGGGTCTTCTCGAACAC), Tgfb (F: GAGCCCAAGCGGACTACTA, R: CACTGCTTCCGAATGTCTGA), Il10 (F: GCCAGACGACATGCTCTCA, R: GTCCAGCTGGTCTTGTGTTG), Nme1 (F: AGGAGACTTCTGCATCCAAGTT, R: TTCTGCGCACAGCTCTTG), Nme6 (F: TGATCAAGCCTGATGCAGTT, R: CGTTCGTACAATGAGGAACCTTG); Suidg1 (F: CACATTCACAAGAAGGGAAGAAT, R: GGTGTTTGGTGAACCTGCTTC).

Statistics. Data are expressed as mean \pm s.e.m. Statistical analysis was performed using a two-tailed Student's *t*-test or ANOVA (with Tukey's post-test analysis) with GraphPad Prism software. A *P* value ≤ 0.05 was considered as statistically significant.

Reporting Summary. Further information on research design is available in the Nature Research Reporting Summary linked to this article.

Data availability

The data that support the findings of this study are available from the corresponding author upon reasonable request. Topological analyses are available at <https://artyomovlab.wustl.edu/shiny/gam/> and at biotest.hematometabolism.science upon request. Raw and processed sequencing data are deposited on the Gene Expression Omnibus under accession code [GSE183176](https://www.ncbi.nlm.nih.gov/geo/query/acc.cgi?acc=GSE183176). Source data are provided with this paper.

Received: 28 September 2020; Accepted: 6 September 2021;
Published online: 14 October 2021

References

- Kojima, Y., Weissman, I. L. & Leeper, N. J. The role of efferocytosis in atherosclerosis. *Circulation* **135**, 476–489 (2017).
- Elliott, M. R. & Ravichandran, K. S. The dynamics of apoptotic cell clearance. *Dev. Cell* **38**, 147–160 (2016).
- Wang, Y. et al. Mitochondrial fission promotes the continued clearance of apoptotic cells by macrophages. *Cell* **171**, 331–345 (2017).
- Yurdagul, A. Jr. et al. Macrophage metabolism of apoptotic cell-derived arginine promotes continual efferocytosis and resolution of Injury. *Cell Metab.* **31**, 518–533 (2020).
- Bosurgi, L. et al. Macrophage function in tissue repair and remodeling requires IL-4 or IL-13 with apoptotic cells. *Science* **356**, 1072–1076 (2017).
- Han, C. Z. & Ravichandran, K. S. Metabolic connections during apoptotic cell engulfment. *Cell* **147**, 1442–1445 (2011).
- DeBerardinis, R. J. & Cheng, T. Q's next: the diverse functions of glutamine in metabolism, cell biology and cancer. *Oncogene* **29**, 313–324 (2010).
- O'Neill, L. A. & Pearce, E. J. Immunometabolism governs dendritic cell and macrophage function. *J. Exp. Med.* **213**, 15–23 (2016).
- Jha, A. K. et al. Network integration of parallel metabolic and transcriptional data reveals metabolic modules that regulate macrophage polarization. *Immunity* **42**, 419–430 (2015).
- Morioka, S. et al. Efferocytosis induces a novel SLC program to promote glucose uptake and lactate release. *Nature* **563**, 714–718 (2018).
- Zhang, S. et al. Efferocytosis fuels requirements of fatty acid oxidation and the electron transport chain to polarize macrophages for tissue repair. *Cell Metab.* **29**, 443–456 (2019).
- Dixon, S. J. et al. Ferroptosis: an iron-dependent form of nonapoptotic cell death. *Cell* **149**, 1060–1072 (2012).
- Nicklin, P. et al. Bidirectional transport of amino acids regulates mTOR and autophagy. *Cell* **136**, 521–534 (2009).
- Tabas, I. Macrophage death and defective inflammation resolution in atherosclerosis. *Nat. Rev. Immunol.* **10**, 36–46 (2010).
- Grabner, R. et al. Lymphotoxin β receptor signaling promotes tertiary lymphoid organogenesis in the aorta adventitia of aged ApoE^{-/-} mice. *J. Exp. Med.* **206**, 233–248 (2009).
- Jais, A. et al. Heme oxygenase-1 drives metaflammation and insulin resistance in mouse and man. *Cell* **158**, 25–40 (2014).
- Vats, D. et al. Oxidative metabolism and PGC-1 β attenuate macrophage-mediated inflammation. *Cell Metab.* **4**, 13–24 (2006).

- Perales-Clemente, E. et al. Restoration of electron transport without proton pumping in mammalian mitochondria. *Proc. Natl Acad. Sci. USA* **105**, 18735–18739 (2008).
- Fernández-Ayala, D. J. et al. Expression of the *Ciona intestinalis* alternative oxidase (AOX) in *Drosophila* complements defects in mitochondrial oxidative phosphorylation. *Cell Metab.* **9**, 449–460 (2009).
- Chandel, N. S. Evolution of mitochondria as signaling organelles. *Cell Metab.* **22**, 204–206 (2015).
- Caron, E. & Hall, A. Identification of two distinct mechanisms of phagocytosis controlled by different Rho GTPases. *Science* **282**, 1717–1721 (1998).
- A-Gonzalez, N. et al. Apoptotic cells promote their own clearance and immune tolerance through activation of the nuclear receptor LXR. *Immunity* **31**, 245–258 (2009).
- Yvan-Charvet, L. et al. ABCA1 and ABCG1 protect against oxidative stress-induced macrophage apoptosis during efferocytosis. *Circ. Res.* **106**, 1861–1869 (2010).
- Viaud, M. et al. Lysosomal cholesterol hydrolysis couples efferocytosis to anti-inflammatory oxysterol production. *Circ. Res.* **122**, 1369–1384 (2018).
- Tavakoli, S. et al. Characterization of macrophage polarization states using combined measurement of 2-deoxyglucose and glutamine accumulation: implications for imaging of atherosclerosis. *Arterioscler Thromb. Vasc. Biol.* **37**, 1840–1848 (2017).
- Johnson, M. O. et al. Distinct regulation of T_H17 and T_H1 cell differentiation by glutaminase-dependent metabolism. *Cell* **175**, 1780–1795 (2018).
- Papathanassiou, A. E. et al. BCAT1 controls metabolic reprogramming in activated human macrophages and is associated with inflammatory diseases. *Nat. Commun.* **8**, 16040 (2017).
- O'Neill, L. A. & Artyomov, M. N. Itaconate: the poster child of metabolic reprogramming in macrophage function. *Nat. Rev. Immunol.* **19**, 273–281 (2019).
- Liu, P. S. et al. α -Ketoglutarate orchestrates macrophage activation through metabolic and epigenetic reprogramming. *Nat. Immunol.* **18**, 985–994 (2017).
- Scialò, F., Fernández-Ayala, D. J. & Sanz, A. Role of mitochondrial reverse electron transport in ROS signaling: potential roles in health and disease. *Front. Physiol.* **8**, 428 (2017).
- Murphy, M. P. How mitochondria produce reactive oxygen species. *Biochem. J.* **417**, 1–13 (2009).
- Lapiente-Brun, E. et al. Supercomplex assembly determines electron flux in the mitochondrial electron transport chain. *Science* **340**, 1567–1570 (2013).
- Guarás, A. et al. The CoQH2/CoQ ratio serves as a sensor of respiratory chain efficiency. *Cell Rep.* **15**, 197–209 (2016).
- Stipanuk, M.H. and Caudill, M.A. *Biochemical, Physiological and Molecular Aspects of Human Nutrition* 3rd edn (Elsevier/Saunders, 2013).
- Jin, H. et al. Integrative multiomics analysis of human atherosclerosis reveals a serum response factor-driven network associated with intraplaque hemorrhage. *Clin. Transl. Med.* **11**, e458 (2021).
- Gautier, E. L. et al. Gene-expression profiles and transcriptional regulatory pathways that underlie the identity and diversity of mouse tissue macrophages. *Nat. Immunol.* **13**, 1118–1128 (2012).
- Devos, M. et al. Keratinocyte expression of A20/TNFAIP3 controls skin inflammation associated with atopic dermatitis and psoriasis. *J. Invest. Dermatol.* **139**, 135–145 (2019).
- Aidoud, N. et al. A combination of lipidomics, MS imaging, and PET scan imaging reveals differences in cerebral activity in rat pups according to the lipid quality of infant formulas. *FASEB J.* **32**, 4776–4790 (2018).

Acknowledgements

We thank B. Caraveo for computational development of DreamBio, a new topological tool for Integrated Network Analysis. N. Grandchamp provided Lenti-ONE AOX vector through GEG Tech. We thank S. Fernandez for the noninvasive study of atheroma plaques by ultrasound echography as part of the European Center for Research in Imaging (Cerimed), F. Labret for assistance with flow cytometry, V. Corcelle for assistance in animal facilities and M. Iroldelle for assistance with confocal microscopy. This work was supported by grants from the Fondation de France, ANR and the European Research Council consolidator program (ERC2016COG724838) to L.Y.-C. CCMA electron microscopy equipment was funded by the Région Sud - Provence-Alpes-Côte d'Azur, the Conseil Départemental des Alpes Maritimes and the GIS-IBISA.

Author contributions

L.Y.-C. conceived the project, designed the experiments and wrote the manuscript. J.M., S.I. and A.D. performed most of the molecular, histological and in vivo experiments. A.S., J.G., M.S., M.A., N.V., A.C., A.S. and A.G. helped with the experimental design and assisted with the data analysis. F.O., T.B. and J.C.M. provided access to platform facilities and assisted with the data acquisition and analysis. S.C., J.M., I.G.S., P.M. and S.R. provided transgenic mice and intellectual discussion. J.C.S. and E.A.L.B. aided in the design and analysis of human studies. R.R. and E.L.G., E.B.T., M.N.A. provided scientific

advice and helped with the experimental design. L.Y.-C. also designed and supervised the study and obtained funding. All of the authors read, edited and approved the manuscript.

Competing interests

The authors declare no competing interests.

Additional information

Extended data is available for this paper at <https://doi.org/10.1038/s42255-021-00471-y>.

Supplementary information The online version contains supplementary material available at <https://doi.org/10.1038/s42255-021-00471-y>.

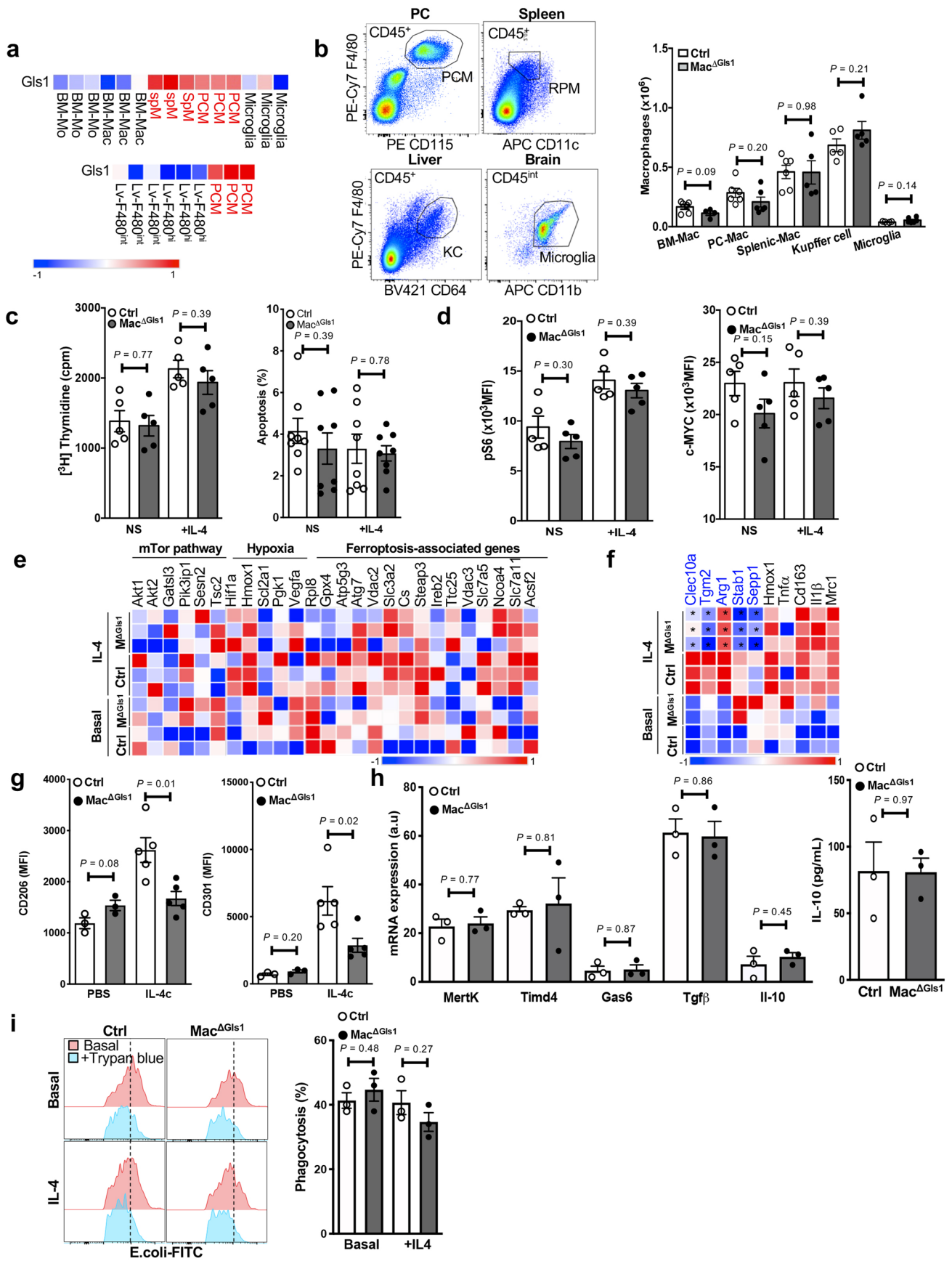
Correspondence and requests for materials should be addressed to Laurent Yvan-Charvet.

Peer review information *Nature Metabolism* thanks Ping-Chih Ho and the other, anonymous, reviewers for their contribution to the peer review of this work. Primary handling editor: George Caputa

Reprints and permissions information is available at www.nature.com/reprints.

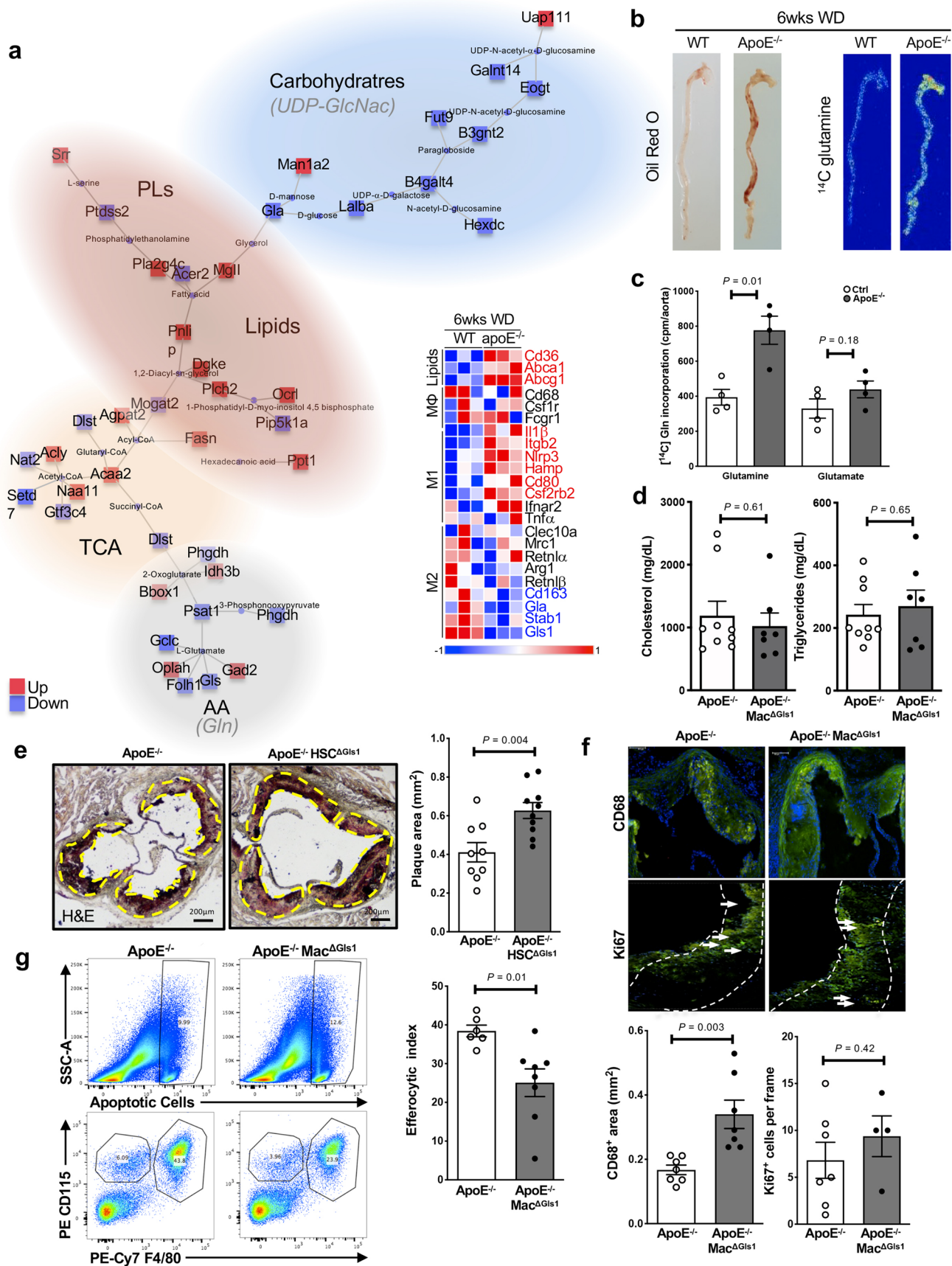
Publisher's note Springer Nature remains neutral with regard to jurisdictional claims in published maps and institutional affiliations.

© The Author(s), under exclusive licence to Springer Nature Limited 2021



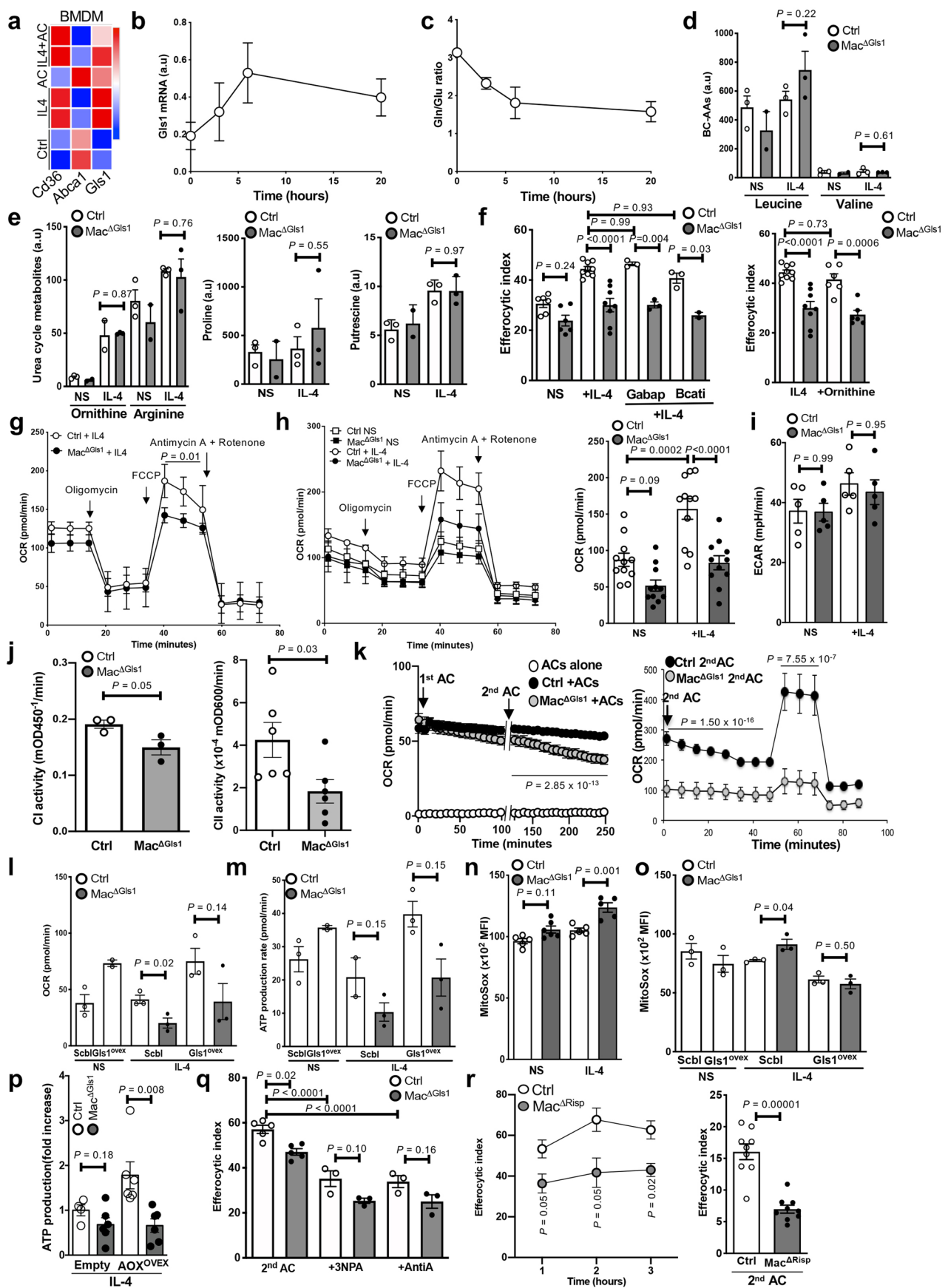
Extended Data Fig. 1 | See next page for caption.

Extended Data Fig. 1 | GLS1 is dispensable for macrophage homeostasis but supports macrophage effector functions. **(a)** Comparative analysis of *Gls1* mRNA expression in different macrophage populations from a publicly available dataset (Immgen). Red indicates up- and blue down-regulated expression **(b)** Macrophage population gating strategy (left) and numbers (right) measured by flow cytometry in multiple mouse tissues (bone marrow, peritoneal cavity, spleen, liver and brain). Both sexes were analyzed. **(c)** [³H]-Thymidine incorporation (left) and apoptosis percentage (right) in *Gls1^{fl/fl}* control or *Mac^{ΔGls1}* macrophages at steady state or after an overnight stimulation with IL-4. **(d)** Phospho-S6 (left) and c-myc (right) expression measured by flow cytometry in these cells. **(e)** RNAseq of control or *Mac^{ΔGls1}* cell sorted PCMs at steady state or after IL-4 stimulation. **(f)** RNAseq analysis with focus on alternatively activated genes in control or *Mac^{ΔGls1}* PCMs stimulated overnight or not with IL-4. **(g)** CD206 and CD301 expression by flow cytometry in *Cre⁺* control or *Mac^{ΔGls1}* mice injected i.p. with PBS or IL-4-complex. **(h)** mRNA expression of key efferocytic receptors such as *MertK*, *Timd4* or *Gas6* or immunoregulatory cytokines such as *Tgfb β* or *Il10* (left panel) or IL-10 secretion (right panel) in reparative *Gls1^{fl/fl}* control and *Mac^{ΔGls1}* PCMs. **(i)** Phagocytosis assays of heat-killed, fluorescently pre-labeled *E.coli* (calculated after quenching the extracellular probe by trypan blue) in these cells. All values are mean \pm SEM and are representative of at least one independent experiment ($n=4$ to 8 independent animals for **b-d**, $n=3$ to 5 for **g-i**). *P* values were determined by a two-tailed Student's t-test. Source data are provided as a Source Data file (**b-d, g-i**).



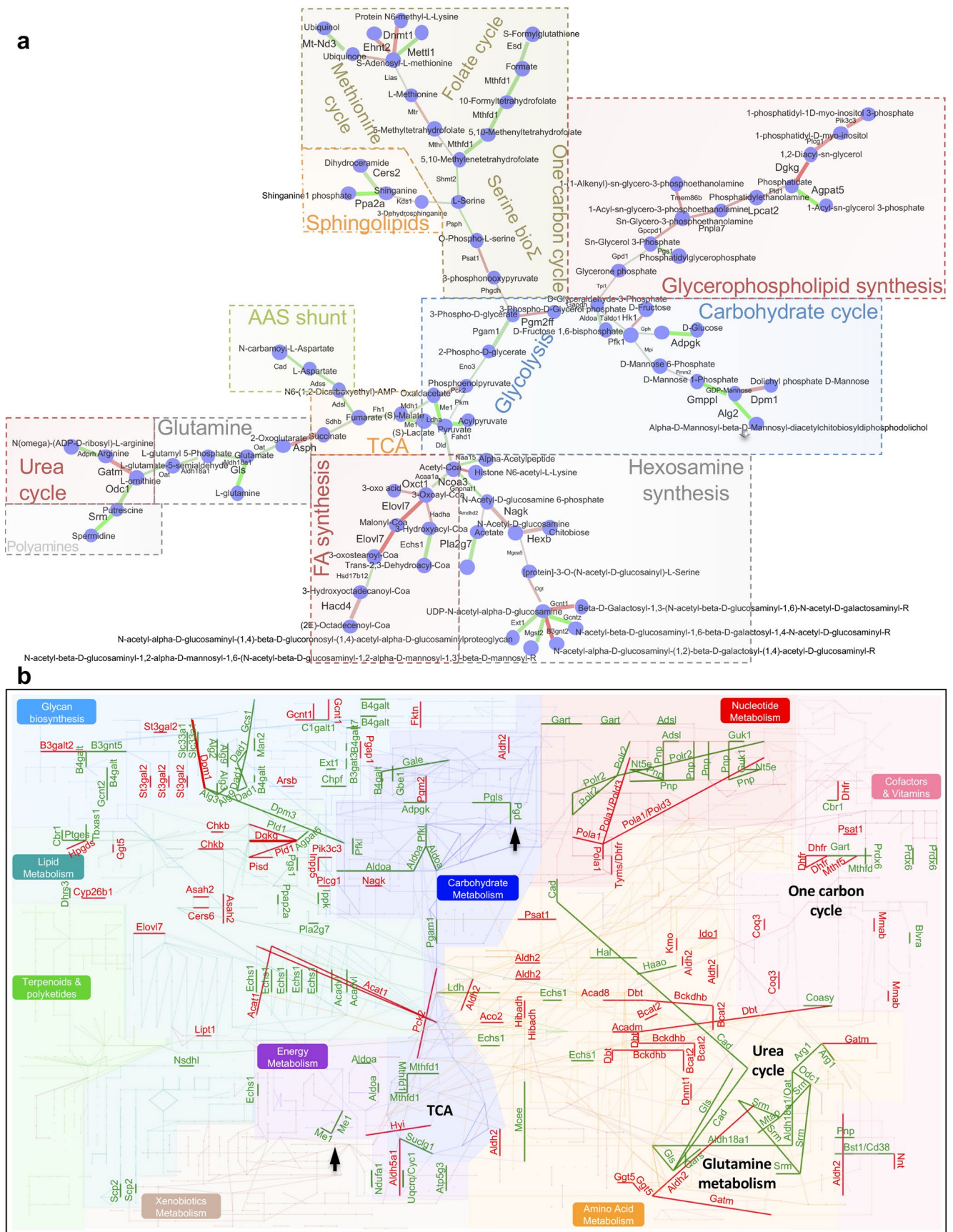
Extended Data Fig. 2 | See next page for caption.

Extended Data Fig. 2 | Atherosclerosis development relies on GLS1-dependent glutaminolysis. (a) Metabolic pathway (left) and RNAseq analysis (right) of *Apoe*^{-/-} versus WT mouse aortas (6 weeks on WD) performed with Phantasus software (GSE10000). Red indicates up- and blue down-regulated expression. (b) Oil red O staining (left) or ¹⁴C glutamine accumulation after i.v. injection (right) in descending aortas extracted from female WT and *Apoe*^{-/-} mice maintained on a WD for 6 weeks. (c) ¹⁴C glutamine incorporation in aortas obtained from female *Apoe*^{-/-} and *Apoe*^{-/-} Mac^{ΔGLS1} mice fed for 6 weeks on WD. (d) Cholesterol (left) and triglyceride (right) content in plasma of *Apoe*^{-/-} and *Apoe*^{-/-} Mac^{ΔGLS1} mice. (e) Representative sections (left) and quantification (right) of aortic plaques from *Apoe*^{-/-} or *Apoe*^{-/-} HSC^{ΔGLS1} mice (12 weeks WD) stained for Oil Red O and Hematoxylin Eosin. Scale bar: 200 μm. (f) Representative sections (top) and quantification (bottom) of aortic plaques from *Apoe*^{-/-} or *Apoe*^{-/-} Mac^{ΔGLS1} mice (12 weeks WD) stained for CD68 and Ki67. (g) Gating strategy (left) and quantification (right) of PCM efferocytic index in *Apoe*^{-/-} and *Apoe*^{-/-} Mac^{ΔGLS1} mice 1-hour after labeled ACs i.p. injection. Both sexes were analyzed. All values are mean ± SEM and are representative of at least one independent experiment (n = 4 independent animals for c, n = 7 to 9 for e-g). P values were determined by a two-tailed Student's t-test. Source data are provided as a Source Data file (c-g).

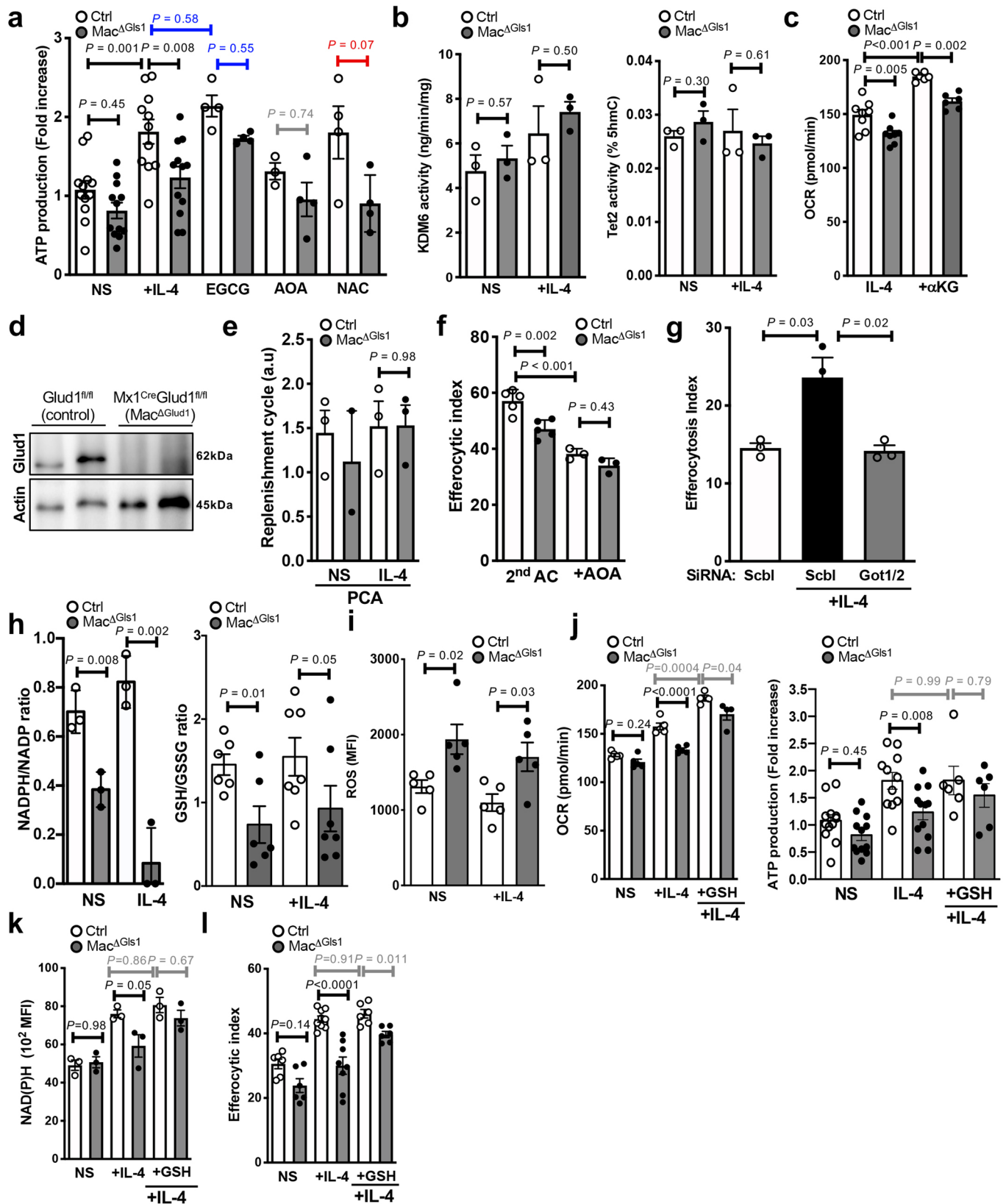


Extended Data Fig. 3 | See next page for caption.

Extended Data Fig. 3 | Glutaminolysis supports mitochondrial OXPHOS and ATP generation to promote efficient efferocytosis. (a) Publicly available gene expression datasets analysis of macrophages ingesting apoptotic cells (GSE98169). Red indicates up- and blue down-regulated expression. (b) *Gls1* mRNA expression and (c) Glutamine/Glutamate ratio during efferocytosis in control BMDMs in a time course experiment. (d) Quantification of leucine and valine levels and (e) ornithine, arginine, proline and putrescine levels in control or $\text{Mac}^{\Delta\text{Gls1}}$ BMDMs at steady state or after IL-4 stimulation. (f) Efferocytic index in control or $\text{Mac}^{\Delta\text{Gls1}}$ BMDMs in basal conditions or stimulated overnight with IL-4 and +/– Gabapentin or Bcat inhibitor (left panel) or treated with IL-4 and ornithine (right panel). (g) OCR measurements in reparative control and $\text{Mac}^{\Delta\text{Gls1}}$ PCMs or (h) in resting and reparative control or $\text{Mac}^{\Delta\text{Gls1}}$ BMDMs. (i) ECAR measured by Seahorse in these BMDMs. (j) Mitochondrial complex I (i.e. NADH-ubiquinone oxidoreductase) (left panel) and complex II (i.e. succinate dehydrogenase (SDH)) (right panel) activities in reparative $\text{Mac}^{\Delta\text{Gls1}}$ BMDMs. (k) OCR measurements after one (45 min) and two (1-hour rest + 45 min) incubations with ACs in control or $\text{Mac}^{\Delta\text{Gls1}}$ BMDMs (resolving condition) (left panel) or after a second incubation with ACs in control or $\text{Mac}^{\Delta\text{Gls1}}$ BMDMs following a standard ‘Seahorse’ procedure (right panel). (l) OCR measurements after empty or *Gls1* lentivirus overexpression in resting control macrophages or reparative control and $\text{Mac}^{\Delta\text{Gls1}}$ BMDMs. (m) ATP production measurements in these cells. (n) Mitochondrial ROS quantification using Mitosox probe in resting and reparative control or $\text{Mac}^{\Delta\text{Gls1}}$ BMDMs and (o) in control and $\text{Mac}^{\Delta\text{Gls1}}$ BMDMs after empty or *Gls1* lentivirus overexpression. (p) ATP production measurements in reparative control or $\text{Mac}^{\Delta\text{Gls1}}$ BMDMs after lentiviral vector-mediated overexpression of empty or mitochondrial alternative oxidase (AOX). (q) Efferocytic index in resolving control or $\text{Mac}^{\Delta\text{Gls1}}$ BMDMs +/– 3NPA or antimycin A between the two rounds of efferocytosis. (r) Efferocytic index after one round efferocytosis (left) or after two round efferocytosis (right) in control or $\text{Risp}^{-/-}$ macrophages. All values are mean \pm SEM and are representative of at least one independent experiment ($n=2$ to 3 independent animals for b–e, $n=3$ to 9 for f–r). *P* values were determined by ordinary two-tailed Student’s *t*-test (d, e, g, j–m, o, p, r) or one-way ANOVA with Tukey post hoc test for multiple comparisons (f, h, i, n, q). Source data are provided as a Source Data file (d–r).

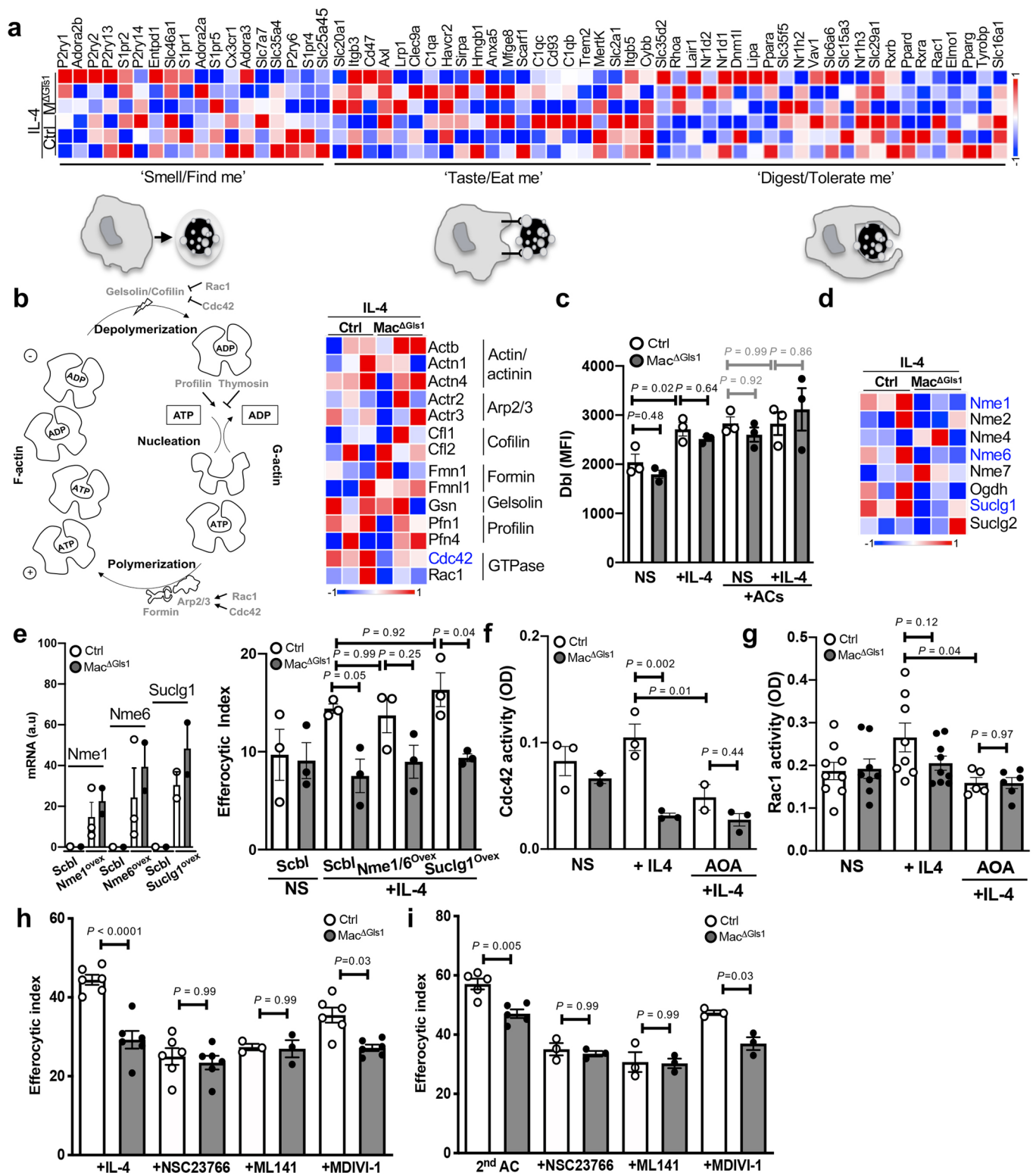


Extended Data Fig. 4 | Gls1 deficiency metabolically reprograms macrophages. (a) CoMBI-T profiling analysis from RNAseq data of reparative IL-4 treated *Gls1*-deficient or sufficient PCMs. **(b)** KEGG mapping with DreamBio from the same RNAseq data. Red indicates up- and green down-regulated expression.

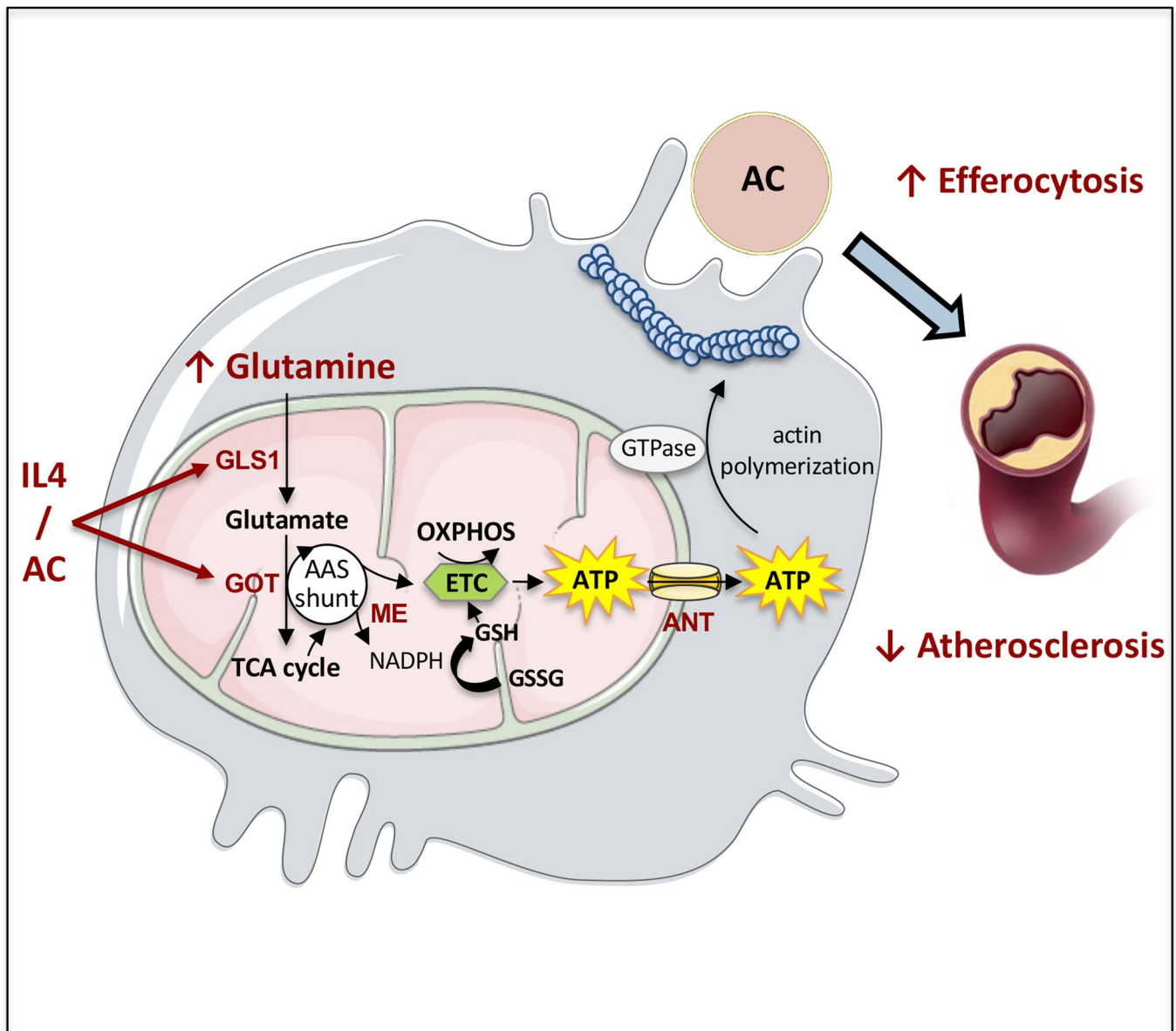


Extended Data Fig. 5 | See next page for caption.

Extended Data Fig. 5 | Gls1 deficiency limits non-canonical transaminase metabolism to modulate OXPHOS and redox balance. **(a)** ATP production measured by Seahorse in control or Mac^{ΔGls1} BMDMs at steady state or after overnight IL-4 stimulation +/- EGCG, AOA or NAC. **(b)** KDM6 activity assay (left) and Tet2 activity assay (right) in resting and reparative control or Mac^{ΔGls1} BMDMs. **(c)** OCR quantification control or Mac^{ΔGls1} BMDMs stimulated overnight with IL-4 in presence or absence of αKetoglutarate. **(d)** GLUD1 protein expression assessed by Western blotting in control or HSC^{ΔGlud1} PCMs. **(e)** Effect of *Gls1* deficiency on PCA (pyroglutamate), a glutathione precursor, as a read out of cellular GSH replenishment. **(f)** Efferocytic index in resolving control or Mac^{ΔGls1} BMDMs +/- AOA treatment between the two rounds of efferocytosis. **(g)** Efferocytic index in control or Mac^{ΔGls1} BMDMs stimulated overnight or not with IL-4 and transfected with scramble or *Got1/Got2* siRNA. **(h)** BMDMs analyzed by liquid chromatography-mass spectrometry. **(i)** ROS quantification using flow cytometry in resting and reparative control or Mac^{ΔGls1} BMDMs. **(j)** OCR quantification and ATP production measured by Seahorse. **(k)** NAD(P)H levels and **(l)** efferocytic index determined by flow cytometry in control or Mac^{ΔGls1} BMDMs in basal conditions or overnight IL-4 stimulation +/- GSH. All values are mean ± SEM and are representative of at least one independent experiment ($n = 3$ to 9 independent animals for **a**, $n = 3$ for **b, e, g, k**, $n = 3$ to 8 for **c, f, h, i, l**, $n = 4$ to 12 for **j**). *P* values were determined by ordinary two-tailed Student's *t*-test (**b, e, g-i**) or one-way ANOVA with Tukey post hoc test for multiple comparisons (**a, f, j-l**). Each statistical bar color-coded represents an independent one-way ANOVA test against IL-4 conditions. Source data are provided as a Source Data file (**a-c, e-l**).



Extended Data Fig. 6 | Glutaminolysis is essential for post-transcriptional regulation of actin dynamics and efferocytosis. (a) Schematic representation of efferocytosis steps and RNAseq analysis of “find-me”, “eat-me” and “tolerate-me” signals in reparative IL-4 treated control and $\text{Mac}^{\Delta\text{Gls1}}$ PCMs. **(b)** Schematic representation of actin polymerization and depolymerization (left panel) and RNAseq analysis with focus on F-actin dynamic regulators in reparative control or $\text{Mac}^{\Delta\text{Gls1}}$ PCMs (right panel). **(c)** Dbl expression quantified by flow cytometry in control or IL-4-treated macrophages that were incubated \pm ACs for 45 min. **(d)** RNAseq analysis with focus on GTP-converting enzymes. **(e)** qPCR quantification (left) and efferocytic index (right) in $\text{Gls}^{\text{fl/fl}}$ control and $\text{Mac}^{\Delta\text{Gls1}}$ BMDMs stimulated overnight with IL-4 after *Nme1/6* or *Suclg1* lentivirus overexpression. **(f)** Cdc42 and **(g)** Rac1 activity assays in control or $\text{Mac}^{\Delta\text{Gls1}}$ BMDMs in basal condition or stimulated overnight with IL-4 \pm AOA. **(h)** Efferocytic index in reparative control or $\text{Mac}^{\Delta\text{Gls1}}$ BMDMs or **(i)** in resolving control or $\text{Mac}^{\Delta\text{Gls1}}$ BMDMs \pm NSC23766 (RAC1 inhibitor), ML141 (CDC42 inhibitor) or MDIVI-1 (DRP1-mediated mitochondrial fission inhibitor). All values are mean \pm SEM and are representative of at least one independent experiment ($n=2$ to 3 independent animals for **c-f**, $n=5$ to 9 for **g**, $n=3$ to 6 for **h, i**). P values were determined by ordinary one-way ANOVA with Tukey post hoc test for multiple comparisons (**c, e-i**). Each statistical bar color-coded represents an independent one-way ANOVA test. Source data are provided as a Source Data file (**c, e-i**).



Extended Data Fig. 7 | Graphical abstract illustrating how non-canonical glutamine transamination sustains efferocytosis in atherosclerotic plaques. Glutaminase (GLS) 1 is upregulated upon reparative (IL-4 stimulation) or resolving (continued clearance of apoptotic cells) to convert glutamine to glutamate. Non-canonical glutamine transamination then acts through the aspartate-arginino-succinate (AAS) shunt to sustain redox buffering (NADPH generation to efficiently supply reduced glutathione GSSG) and fuel energy (i.e. ATP) production through efficient oxidative phosphorylation for cytoskeletal rearrangements.

Reporting Summary

Nature Research wishes to improve the reproducibility of the work that we publish. This form provides structure for consistency and transparency in reporting. For further information on Nature Research policies, see our [Editorial Policies](#) and the [Editorial Policy Checklist](#).

Statistics

For all statistical analyses, confirm that the following items are present in the figure legend, table legend, main text, or Methods section.

n/a Confirmed

- The exact sample size (n) for each experimental group/condition, given as a discrete number and unit of measurement
- A statement on whether measurements were taken from distinct samples or whether the same sample was measured repeatedly
- The statistical test(s) used AND whether they are one- or two-sided
Only common tests should be described solely by name; describe more complex techniques in the Methods section.
- A description of all covariates tested
- A description of any assumptions or corrections, such as tests of normality and adjustment for multiple comparisons
- A full description of the statistical parameters including central tendency (e.g. means) or other basic estimates (e.g. regression coefficient) AND variation (e.g. standard deviation) or associated estimates of uncertainty (e.g. confidence intervals)
- For null hypothesis testing, the test statistic (e.g. F , t , r) with confidence intervals, effect sizes, degrees of freedom and P value noted
Give P values as exact values whenever suitable.
- For Bayesian analysis, information on the choice of priors and Markov chain Monte Carlo settings
- For hierarchical and complex designs, identification of the appropriate level for tests and full reporting of outcomes
- Estimates of effect sizes (e.g. Cohen's d , Pearson's r), indicating how they were calculated

Our web collection on [statistics for biologists](#) contains articles on many of the points above.

Software and code

Policy information about [availability of computer code](#)

Data collection

FACS DIVA Software v8.0.3
Illumina Beadstudio v3 Gene expression software
StepOne device v2.3
TyphoonTM Biomolecular Imager
HiSeq 2500 (Illumina)

Data analysis

Tree Star, FlowJo v10.8
ImageJ
Phantasus v1.11.0
GraphPad Prism8 v8.2.1
StepOne Software v.2.3
R Bioconductor lumi package.2 Limma R package
DreamBio
Shiny Gam 0.99.5-8-gec900f3
MATLAB
PARADISE software
Seahorse XF report generator wave2.4.1

For manuscripts utilizing custom algorithms or software that are central to the research but not yet described in published literature, software must be made available to editors and reviewers. We strongly encourage code deposition in a community repository (e.g. GitHub). See the Nature Research [guidelines for submitting code & software](#) for further information.

Data

Policy information about [availability of data](#)

All manuscripts must include a [data availability statement](#). This statement should provide the following information, where applicable:

- Accession codes, unique identifiers, or web links for publicly available datasets
- A list of figures that have associated raw data
- A description of any restrictions on data availability

The data that support the findings of this study are available from the corresponding author upon reasonable request. Raw and processed sequencing are deposited to PubMed GEO under GSE183176.

Field-specific reporting

Please select the one below that is the best fit for your research. If you are not sure, read the appropriate sections before making your selection.

- Life sciences Behavioural & social sciences Ecological, evolutionary & environmental sciences

For a reference copy of the document with all sections, see [nature.com/documents/nr-reporting-summary-flat.pdf](https://www.nature.com/documents/nr-reporting-summary-flat.pdf)

Life sciences study design

All studies must disclose on these points even when the disclosure is negative.

Sample size	The numbers of samples are indicated in the figure legends for each panel. For atherosclerosis studies, sample size was estimated for a 80% chance of a 30% difference in atherosclerotic lesion area using the power calculation where $P < 0.05$.
Data exclusions	Not expected outliers were found in figures Fig. 3d and Fig. S3g using GraphPad QuickCalcs but their presence or removal did not affect statistical significance.
Replication	All attempts at replication were successful. Findings were replicated in at least three biological independent samples each.
Randomization	Allocation of samples were random. Otherwise, animals were placed into separate groups according to their genotype.
Blinding	Where possible, Investigators were blinded to group allocation during data collection and analysis for figures 2a, 2c, 5d, 5f, s2b, s2e, s2f.

Reporting for specific materials, systems and methods

We require information from authors about some types of materials, experimental systems and methods used in many studies. Here, indicate whether each material, system or method listed is relevant to your study. If you are not sure if a list item applies to your research, read the appropriate section before selecting a response.

Materials & experimental systems

n/a	Involved in the study
<input type="checkbox"/>	<input checked="" type="checkbox"/> Antibodies
<input checked="" type="checkbox"/>	<input type="checkbox"/> Eukaryotic cell lines
<input checked="" type="checkbox"/>	<input type="checkbox"/> Palaeontology and archaeology
<input type="checkbox"/>	<input checked="" type="checkbox"/> Animals and other organisms
<input type="checkbox"/>	<input checked="" type="checkbox"/> Human research participants
<input checked="" type="checkbox"/>	<input type="checkbox"/> Clinical data
<input checked="" type="checkbox"/>	<input type="checkbox"/> Dual use research of concern

Methods

n/a	Involved in the study
<input checked="" type="checkbox"/>	<input type="checkbox"/> ChIP-seq
<input type="checkbox"/>	<input checked="" type="checkbox"/> Flow cytometry
<input checked="" type="checkbox"/>	<input type="checkbox"/> MRI-based neuroimaging

Antibodies

Antibodies used

Anti- α -actine HRP Santa Cruz sc-32251HRP 1/10000
 Anti-CD68 (clone FA-11) Bio-Rad MCA1957 1/200
 Anti-Glut1 Abcam ab166618 1/500
 Anti-Glutaminase Abcam ab93434 1/500
 Anti-IL-4 (clone 11B11) BioXcell BE0045 25ug/mice
 Anti-Ki67 PE (clone 16A8) Biolegend 652403 1/200
 Anti-Rat Alexa Fluor 488 ThermoFisher A-11006 1/1000
 c-Myc PE (Clone D84C12) Cell Signaling 14819S 1/100
 CD115 PE (clone AFS98) eBioscience 12-1152-82 1/200
 CD11b Brilliant Violet 510 (cloneM1/70) Biolegend 101263 1/200
 CD11c APC (clone N418) BD Biosciences 117309 1/200

CD206 PerCp-Cy5.5 (clone C068C2) Biolegend 141715 1/50
 CD301 FITC (clone ER-MP23) Bio-RadMCA2392 1/200
 F4/80 AF488 (clone BM8) Biolegend 123120 1/200
 CD45 APC-Cy7 (clone 30-F11)BD Biosciences 557659 1/200
 CD64 Brilliant Violet 421 (clone X54-5/7.1) Biolegend 139309 1/200
 F4/80 PE-Cy7 (clone BM8) Biolegend 123114 1/200
 ICAM-2 alexa fluor 647 (clone 3C4(MIC2/4)) Biolegend 105612 1/200
 MerTK PE (clone 2B10C42) Biolegend 151506 1/200
 PD-L2 APC (clone B7-DC) Biolegend 107210 1/200
 Phalloidine Alexa Fuor 594 InVitrogen A12381 1/200
 Phospho-S6 Ribosomal Protein (ser235/236) PE (clone D57.2.2E) Cell Signaling 5316S 1/100
 Tim4 PE-Cy7 (clone RMT4-54) Biolegend 130010 1/200
 Horseradish peroxidase conjugated secondary anti-Rabbit (#7074) Cell Signaling technologies 1/5000

Validation

Antibodies were used according to manufacturers instructions. Antibody validations were performed by antibody suppliers per quality assurance literature provided by each supplier.

Animals and other organisms

Policy information about [studies involving animals](#); [ARRIVE guidelines](#) recommended for reporting animal research

Laboratory animals

8-14 weeks male and female mice were used for ex-vivo and in-vivo experiments. Gls1fl/fl mice were kindly provided by Pr. Stephen Rayport (Glstm2.1Sray/J deposited at The Jackson Laboratory) and have been crossed to Lyz2Cre mice (B6.129P2-Lyz2tm1(cre)lfo/J, The Jackson Laboratory) or Mx1cre mice (B6.Cg-Tg(Mx1-cre)1Cgn/J) and brought on ApoE-deficient genetic background (B6.129P2-ApoEtm1Unc/J). Mx1cre mice (B6.Cg-Tg(Mx1-cre)1Cgn/J) were also crossed to C57BL/6 Glud1 floxed mice (kindly provided by Pr. Pierre Maechler). Animals had free access to food (chow diet A04, SafeR) and water and were housed in a controlled environment with a 12-hour light-dark cycle, constant temperature (22°C) and relative humidity (50-60%).

Wild animals

No wild animals were used in this study.

Field-collected samples

No field-collected samples were used in this study.

Ethics oversight

Animal protocols were approved by the Institutional Animal Care and Use Committee of the French Ministry of Higher Education and Research and the Mediterranean Center of Molecular Medicine (Inserm U1065) and were undertaken in accordance with the European Guidelines for Care and Use of Experimental Animals.

Note that full information on the approval of the study protocol must also be provided in the manuscript.

Human research participants

Policy information about [studies involving human research participants](#)

Population characteristics

Symptomatic patients undergoing carotid endarterectomy (CEA) in the Maastricht human plaque study (MaasHPS) were recently described (Jin, H. et al. Clin Transl Med 2021 PMID 34185408). Briefly, Age (72.9 ± 6.3 years, mean ± SD); Age range (64 - 83 years); Current or prior smoking (35%); Arterial hypertension (65%); Hyperlipidemia (65%); Diabetes mellitus (22%); Medication lipid-lowering (57%); Medication anti-hypertensive (65%); Medication anti-coagulant (100%); Medication anti-inflammation (26%); Cholesterol level Total (mmol/L, 4.7 ± 1.1, mean ± SD).

Recruitment

N/A (from pre-existing stored samples)

Ethics oversight

Tissue collection was part of the Maastricht Pathology Tissue Collection (MPTC) and further storage and use of the tissue was in line with the Dutch Code for Proper Secondary use of Human Tissue and the local Medical Ethical Committee (protocol number 16-4-181). The Maastricht human plaque study (MaasHPS) is associated with Department of Pathology, Cardiovascular Research Institute Maastricht, Maastricht University Medical Center, Maastricht, the Netherlands

Note that full information on the approval of the study protocol must also be provided in the manuscript.

Flow Cytometry

Plots

Confirm that:

- The axis labels state the marker and fluorochrome used (e.g. CD4-FITC).
- The axis scales are clearly visible. Include numbers along axes only for bottom left plot of group (a 'group' is an analysis of identical markers).
- All plots are contour plots with outliers or pseudocolor plots.
- A numerical value for number of cells or percentage (with statistics) is provided.

Methodology

Sample preparation

For full description, please refer to the Method section of the manuscript. Briefly, tissues were excised after PBS

Sample preparation

(Thermo Fisher Scientific) perfusion. Bone marrow cells were collected by flushing bones with PBS after which a single cell suspension was created by passing cells through a 26-gauge needle. Peritoneal leukocytes were harvested by PBS lavage. Spleens were crushed through a 40mm cell strained. Liver and brain were minced and digested with 1.5mg/ml collagenase D (Sigma-Aldrich) in HBSS for 30 minutes at 37°C. Red blood cells were lysed with RBC lysis buffer.

Instrument

Data were acquired on a BDFACSCanto

Software

FlowJo

Cell population abundance

Post sort, cell abundance was sufficient for down stream applications. After sorting, a small fraction of the sorted cells were run through BDFACSCanto and the same gating strategy was applied to check the purity of sorted cell populations. A general purity of higher than 95% were achieved for all the sorted population.

Gating strategy

FSC/SSC gating was used to exclude dead cells and debris followed by FSCA/FSCH to select singlets. Gating strategy for all viable cells have been carefully illustrated and described in the manuscript.

Tick this box to confirm that a figure exemplifying the gating strategy is provided in the Supplementary Information.